Autonomous Asteroid Characterization through Nanosatellite Swarming

Nathan Stacey
Dept. of Aeronautics & Astronautics
Stanford University
Stanford, CA 94305
nstacey@stanford.edu

Kaitlin Dennison
Dept. of Aeronautics & Astronautics
Stanford University
Stanford, CA 94305
kdenn@stanford.edu

Simone D'Amico
Dept. of Aeronautics & Astronautics
Stanford University
Stanford, CA 94305
damicos@stanford.edu

***Abstract*—This paper develops a novel algorithmic framework for autonomous asteroid characterization for the Autonomous Nanosatellite Swarming (ANS) mission concept. There is significant interest in asteroids as evidenced by multiple completed and ongoing asteroid missions. However, these missions heavily rely on human oversight and Earth-based resources such as the NASA Deep Space Network. Such an approach is not sustainable in the long term due to cost and oversubscribed Earth-based resources. Furthermore, these missions typically utilize a single spacecraft that is slow to adapt to its environment due to light time delay and gaps in communication with the Earth. In contrast, ANS comprises multiple small spacecraft that operate autonomously after a brief ground-in-the-loop initialization. The spacecraft are equipped with low size, weight, power, and cost (SWaP-C) avionics including star trackers, short-range cameras, radio-frequency intersatellite links, and chip scale atomic clocks. The algorithmic framework developed in this paper utilizes the intersatellite links and images of the asteroid to simultaneously estimate the spacecraft states as well as the asteroid gravity field, shape, and rotational motion. This class of estimation problem is defined in this paper as simultaneous navigation and characterization (SNAC), which is a superset of simultaneous localization and mapping. The ANS SNAC framework consists of three novel modules: 1) multi-agent optical landmark tracking and 3D point reconstruction using stereovision, 2) state estimation through a computationally efficient and robust unscented Kalman filter, and 3) reconstruction of a global spherical harmonic shape model by leveraging a priori knowledge of the shape properties of small celestial bodies. This new framework is validated through the numerical simulation of three spacecraft orbiting the asteroid 433 Eros. The simulation results demonstrate that the proposed architecture provides autonomous and accurate SNAC in a safe manner without any a priori shape model and using only low SWaP-C avionics.**

TABLE OF CONTENTS

978-1-6654-3760-8/22/$31.00 ©2022 IEEE

1. INTRODUCTION

Asteroids provide insight into the formation of the solar system and may hold clues to the origin of life [1, 2]. Moreover, further study of asteroids may enable the utilization of their resources and the prevention of future asteroid-Earth collisions [3, 4]. Asteroid missions to date such as NEAR Shoemaker [5], Dawn [6], OSIRIS-REx [7], and the Hayabusa missions [8, 9] have provided a wealth of knowledge. However, completed missions have depended extensively on human oversight and highly solicited Earth-based resources such as the NASA Deep Space Network. This approach is expensive and the spacecraft is slow to react to its environment due to light time delay and gaps in communication with the Earth. To address these limitations, this paper develops the distributed navigation, time synchronization, and asteroid characterization framework of the Autonomous Nanosatellite Swarming (ANS) mission concept [10]. ANS is an autonomous swarm of small satellites that cooperate to characterize an asteroid using intersatellite radio-frequency (RF) measurements and optical landmark tracking. Through autonomy and small satellite technology, ANS improves performance and reduces mission cost, thus enabling a greater number of future small body missions.

In order for a mission operating in close proximity to an asteroid to safely achieve its objectives, the spacecraft state relative to the asteroid must be estimated as well as the asteroid gravity field, shape, and rotational motion. This task belongs to a new class of estimation problem defined in this paper as simultaneous navigation and characterization (SNAC) [10]. SNAC is a superset of simultaneous localization and mapping (SLAM) [11]. While SLAM concurrently estimates a physical map of the environment and the location of an agent within that map, SNAC can also include the estimation of additional characteristics of the environment and of other agents. For example, SNAC would include the navigation of a spacecraft and the simultaneous characterization of the physical properties, maneuvers, or objectives of a nearby noncooperative spacecraft. In the context of this work, SNAC includes estimating the asteroid gravity field, global shape, and rotational motion. These SNAC estimates enable safe and fuel efficient operations in proximity to the asteroid, facilitate landing site selection, and yield important scientific insights.

To achieve SNAC, completed asteroid missions have required significant human oversight and hours of daily radiometric tracking and communication using Earth-based resources [5, 6, 12, 13]. These missions also tend to rely on offline al-

gorithms that are too computationally expensive for onboard implementation such as stereo-photoclinometry [14, 15] and batch orbit determination techniques [12]. Additionally, high size, weight, power, and cost (SWaP-C) avionics are commonly used such as lidar [16].

In order to make asteroid missions more sustainable and cost effective, there have been efforts to increase autonomy [10, 17–22]. One interesting semi-autonomous concept uses hopping rovers deployed by an orbiting spacecraft [23, 24]. Some proposed autonomous mission concepts utilize hyperbolic trajectories [20–22], which only provide coarse asteroid characterization due to the short time in proximity to the asteroid. Most studies of autonomous asteroid mission concepts use significant simplifying assumptions such as idealized image processing, time-keeping, and estimation as well as the absence of process noise and sensor biases [10, 17, 18]. Some autonomous mission concepts also require an accurate a priori gravity or shape model [18, 25].

Many proposed asteroid mission architectures increase autonomy through distributed space systems (i.e., multiple cooperative spacecraft) [17,18,20,21]. Distributed space systems are promising for asteroid SNAC because they can often achieve objectives that would be cumbersome or impossible for a traditional single spacecraft mission. Advantages of distributed space systems include greater robustness, accuracy, flexibility, and sensing coverage. Salient examples of missions that are enabled by distributed space systems include GRACE (NASA) [26], TanDEM-X (DLR) [27], and MMS (NASA) [28] as well as future missions such as Starling [29], mDOT [30], SWARM-EX [31], and VISORS [32]. Distributed space systems often leverage recent advances in small spacecraft technology. In particular, the MarCO two-spacecraft mission recently demonstrated the first use of CubeSats in deep space [33].

Autonomous navigation for distributed space systems has been studied and tested extensively in Earth-orbit [34], and has been investigated for interplanetary missions for the recently proposed ARTMS navigation payload on the Starling mission [35]. Simple autonomous navigation was briefly used for the Deep Impact distributed space mission to the comet Tempel 1. The Deep Impact probe released an impactor that used autonomous optical navigation to collide with the comet [36]. However, to the authors' knowledge no current single or multi-spacecraft autonomous asteroid mission concept can achieve SNAC, including estimation of the asteroid gravity field, global shape, and rotational motion, using only onboard low SWaP-C avionics and without an a priori shape model.

ANS achieves autonomous SNAC through multiple small satellites equipped with low SWaP-C hardware including star trackers, chip scale atomic clocks, short-range cameras, and intersatellite RF links. The spacecraft are in closed, reconfigurable orbits about the target asteroid, which provides a geometrically diverse set of measurements over a long period of time. After a brief ground-in-the-loop initialization phase, the spacecraft autonomously characterize the asteroid. No a priori shape model is required. This paper develops the ANS SNAC architecture and is a significant improvement upon the authors' prior work on ANS [10, 37].

Specifically, this paper has four main contributions. First, a multi-agent optical landmark tracking and stereovision approach is developed using images from the satellite short-range cameras. The low SWaP-C nature of cameras makes them well suited to small spacecraft and is a significant advantage over many other types of sensors such as lidar and radar. Second, a computationally efficient and robust unscented Kalman filter (UKF) is presented. Third, a novel method is presented to estimate a global spherical harmonic shape model from landmark point estimates by leveraging a priori knowledge of the shape characteristics of small celestial bodies. The spherical harmonic shape model is particularly powerful when paired with the estimated spherical harmonic gravity model because characteristics of the asteroid mass distribution can be inferred [38]. Moreover, the shape model can be used to maintain a safe distance from the asteroid and enables the use of a polyhedral gravity model, which can be utilized close to the asteroid where a spherical harmonic gravity model may diverge [39]. Fourth, the ANS SNAC architecture is validated through high-fidelity software simulations including the most relevant sources of uncertainty.

Following this introduction, Section 2 details the ANS concept of operations. This section is intended to provide operational context, but it does not diminish the generality of the new algorithms. Section 3 describes the process for optically tracking landmarks and reconstructing them in 3D space using stereovision. Section 4 describes how optical pixel measurements of landmarks are fused with intersatellite RF measurements in a computationally efficient and robust manner to estimate the spacecraft states and asteroid properties. A novel technique is presented in Section 5 for global asteroid shape reconstruction from landmark point estimates. In Section 6, the developed SNAC algorithmic architecture is validated through the numerical simulation of three spacecraft orbiting the asteroid 433 Eros. Finally, conclusions are presented in Section 7 based on the numerical results.

2. CONCEPT OF OPERATIONS

ANS consists of a mothership and one or more deputy nanosatellites, all of which cooperate to characterize an asteroid (see Figure 1). The mothership has greater computation power and is the only spacecraft equipped with a high-gain antenna to communicate with the Earth, primarily at the beginning and end of the mission or at major intermediate milestones. Although some computational tasks are executed exclusively on the mothership, the image processing is distributed among the swarm in order to reduce the maximum computational burden on any one spacecraft. The proposed algorithmic subsystems and intersatellite data transfer are depicted in Figure 2.

The low SWaP-C sensors onboard each spacecraft are a short-range camera, an intersatellite RF link, a chip scale atomic clock, and a star tracker. Potential small spacecraft avionics can be found in [40]. The short-range cameras are used to optically detect and track asteroid landmarks. The star trackers provide inertial attitude solutions for each spacecraft. The intersatellite RF links between every pair of spacecraft provide intersatellite one-way pseudorange and Doppler measurements while facilitating communication and data transfer.

Data transfer from the deputy spacecraft to the mothership includes the intersatellite pseudorange and Doppler measurements, inertial attitude solutions, and landmark pixel measurements and feature descriptors. Landmark detection and inertial attitude solutions are computed by each individual spacecraft. Thus, the computational load is distributed among the swarm. Additionally, the total data transfer load between

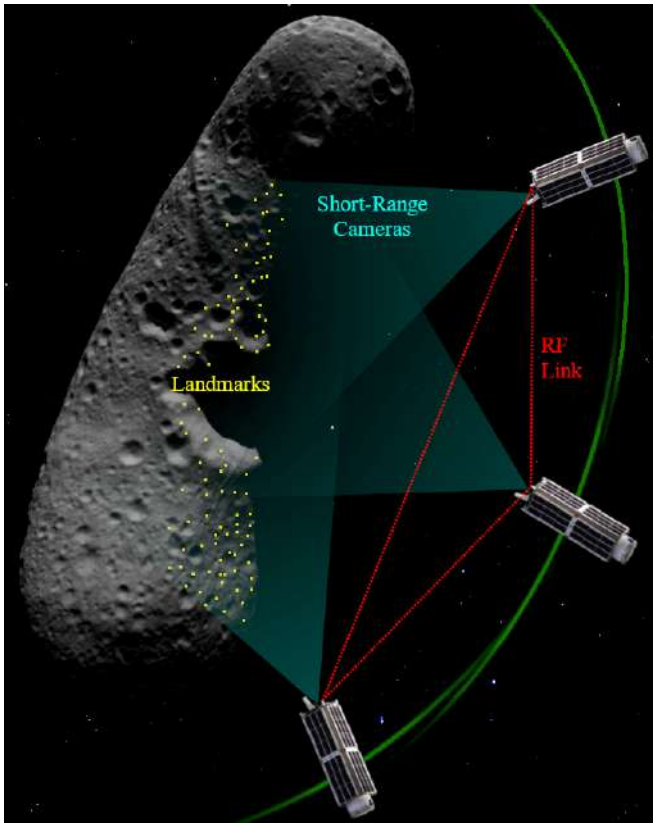

Figure 1. Conceptual illustration of ANS including the spacecraft orbits, intersatellite RF links, and landmarks tracked using the spacecraft short-range cameras.

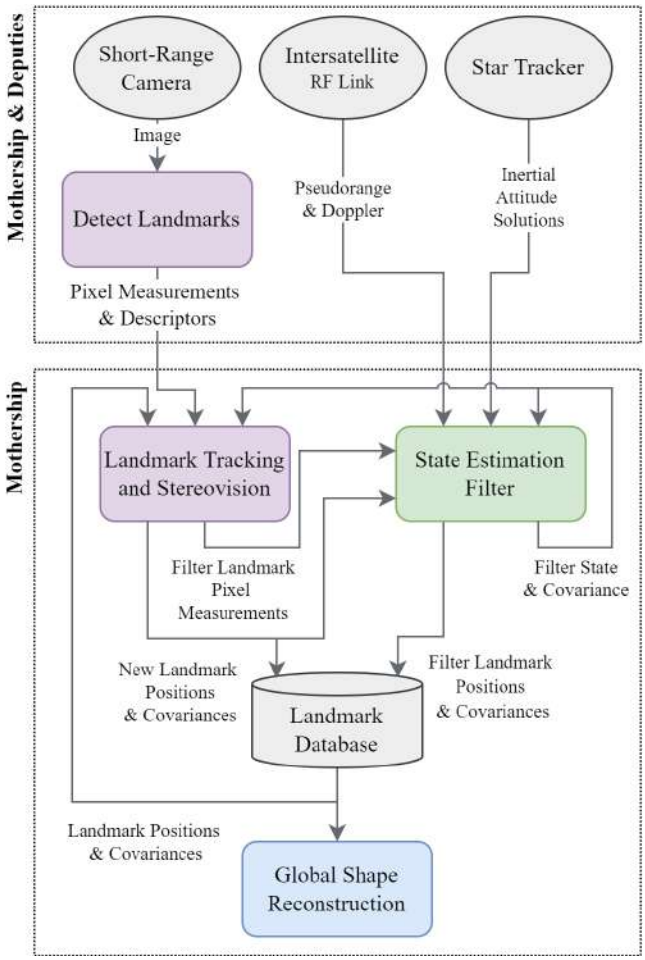

Figure 2. ANS data transfer and system interactions to perform SNAC. The ovals are sensors, the rectangles are algorithms, and the cylinder represents data storage.

spacecraft is reduced by transferring landmark pixel measurements and feature descriptors instead of full images. The primary data transferred from the mothership to the deputies relates to maneuver commands. Guidance and control (e.g., [41]) are not considered in this paper and are, therefore, not illustrated in Figure 2. A landmark database is stored on the mothership and is depicted by the cylinder in Figure 2. The landmark database includes the 3D asteroid-centered asteroid-fixed (ACAF) positions and associated error covariances of landmarks that are currently tracked in the filter state and landmarks that have been retired (i.e., removed and stored) from the filter state. The coordinate frames used throughout this paper are defined in Table 1.

The swarm orbit geometry is designed to provide safe and accurate asteroid characterization. The mean semi-major axis of each spacecraft is equal to prevent the swarm from quickly drifting apart in the along-track direction. The spacecraft are primarily separated in the along-track direction by a distance that provides passive collision avoidance and balances two competing interests. On one hand, decreasing intersatellite separation improves correlation of 2D keypoints between images taken by different spacecraft at approximately the same epoch. On the other hand, increasing intersatellite separation increases the accuracy of stereovision and the observability provided by landmark pixel measurements to the estimation filter. A conceptual depiction of this formation and the spacecraft sensors is shown in Figure 1.

SNAC Algorithmic Architecture

Upon initial approach, a brief ground-in-the-loop phase uses optical navigation and ground-based radiometric tracking to get coarse initial estimates of the spacecraft states, the asteroid rotational parameters, and the asteroid gravity field spherical harmonic coefficients. This phase can be accomplished similarly to completed missions [7,15] and is assumed to have already been done in this paper. After the ground-in-the-loop initialization, the swarm autonomously tracks landmarks, updates the landmark database, and simultaneously estimates the spacecraft states and asteroid properties. This process is divided into three algorithmic subsystems as illustrated in Figure 2.

The first subsystem comprises both purple blocks in Figure 2 and is discussed in Section 3. This subsystem detects landmarks, tracks them over time, and initializes the 3D positions of new landmarks. Keypoint detection identifies unique landmarks in each image. Scale-invariant feature transform (SIFT) [42] keypoint detection is used to detect potential landmarks in images. Previous studies have shown that SIFT is the most reliable detection method when compared to other keypoint descriptors, including crater tracking, in the asteroid environment where lighting and perspective changes between images can be significant [37, 43]. Landmarks are tracked in two ways. The first method correlates landmarks between

Table 1. Coordinate frame definitions. If unspecified, the third axis completes the right-handed triad.

Frame	Definition
ACAF	Asteroid-Centered Asteroid-Fixed
	X-axis aligned with asteroid prime meridian
	Z-axis aligned with asteroid mean spin axis
ACI	Asteroid-Centered Inertial
	X-axis aligned with vernal equinox
	Z-axis normal to Earth mean-equatorial plane
ACIC	Asteroid-Centered Inertial Control
	X-axis aligned with ACAF x-axis at J2000 epoch
	Z-axis aligned with asteroid mean spin axis
CF	Camera Fixed
	X-axis parallel to image plane pixel columns
	Y-axis parallel to image plane pixel rows
	Z-axis aligned with camera boresight
RTN	Radial Transverse Normal
	R-axis aligned with s/c position vector
	N-axis aligned with s/c angular momentum vector

images taken at the same nominal epoch by each spacecraft. This method uses only the similarity of keypoint feature descriptors as a correlation metric [42]. The second method correlates landmarks actively maintained in the estimation filter state to keypoints detected in the images taken by each spacecraft. This method uses both the feature descriptors and the Mahalanobis distance between the feature 2D pixel location and the expected location based on the filter output [11].

Immediately after the ground-in-the-loop initialization, the landmark database is empty. Landmark pixel measurements are reconstructed in 3D space to provide initial ACAF landmark position estimates to the filter. Neither lidar, nor radar, nor an initial shape model is used to aid in reconstruction. Instead, multi-agent stereovision is used to reconstruct landmark 3D positions from the pixel locations of keypoints matched between images recorded by two different spacecraft and based on the filter estimates of the spacecraft states and asteroid rotational parameters [44]. Although multi-agent stereovision is commonly used for planetary exploration with ground-based robots [45] and unmanned aerial vehicles [46], stereovision has only been performed in space using a single spacecraft or in batch-processing of asteroid images [47, 48].

The second subsystem is state estimation, which is shown in green in Figure 2. This subsystem is only executed on the mothership and is described in Section 4. This subsystem fuses the pixel measurements of tracked landmarks with intersatellite RF measurements in a UKF to simultaneously estimate the spacecraft states, landmark 3D positions, and asteroid characteristics. A coarse initial filter state estimate and covariance is provided by the ground-in-the-loop initialization. However, no initial estimates of landmark positions are required. After the ground-in-the-loop initialization, stereovision estimates of new landmark 3D ACAF positions from the first subsystem are added to the filter state. SIFT keypoint descriptors cannot reliably locate the same physical feature when there are significant changes in perspective and illumination conditions [42]. Thus, landmarks that have not been observed for a specified amount of time are removed from the filter state. As a result, the number of landmarks in the filter state varies over time as they are added and removed. However, knowledge of the landmark 3D positions and uncertainties is retained in the landmark database (see Figure 2). In fact, after each filter call the landmark database is updated with the current mean state estimates and covariances of the landmarks currently in the filter state. The UKF runtime is reduced with no loss of accuracy and is made robust to dynamics modeling deficiencies through the recently developed exploiting triangular structure and adaptive state noise compensation techniques [10, 49]. Measurement underweighting is used initially to provide robustness to measurement nonlinearities.

The third subsystem is global shape reconstruction, which is shown in blue in Figure 2 and is only executed on the mothership. This subsystem generates a global asteroid shape model through a least squares fit of the coefficients of a spherical harmonic shape model to the estimated landmark positions in the landmark database. Each landmark estimate is weighted according to its uncertainty. A novel regularization procedure leveraging a priori knowledge of the power spectra of spherical harmonic shape coefficients of small celestial bodies is used. This regularization prevents overfitting and provides accurate shape reconstruction between landmark point estimates. This subsystem is described in detail in Section 5.

3. LANDMARK TRACKING AND STEREOVISION

State estimation requires the pixel measurements of as many landmarks in the filter state as possible to perform an update. However, as the asteroid rotates and the spacecraft continue in their orbits, landmarks enter and leave the field of view. Thus, new landmarks must be added to the filter and obsolete ones must be removed. The landmark tracking and stereovision subsystem accomplishes this in three steps. The first step is to correlate landmarks already in the filter state to the keypoints in the image taken by each spacecraft. The second step is to initialize new landmark estimates to be added to the filter state. This requires correlating keypoints between two images taken at the same time step and reconstructing them in the ACAF frame in order to provide an initial 3D state to the filter. These keypoint pairs are projected into 3D space using stereovision. The final step is to determine which landmarks to retire from the filter state and how to maintain the database of landmarks. The landmark tracking and stereovision subsystem occurs after the filter time update but before the measurement update so the filter mean state estimate and associated covariance are at the same nominal epoch as the images.

Step One: Correlate Filter Landmarks

In the first step of landmark tracking and stereovision, landmarks from the filter state are correlated to the keypoints in the images captured by the spacecraft at the same nominal epoch. Mahalanobis distance and the Euclidean norm between consecutive keypoint descriptors are used as the correlation metrics. For each spacecraft, all of the filter landmarks are iterated over to identify correlations. This subsection describes one iteration of this process, which determines which keypoint k^*, if any, correlates to the ith filter landmark in the image from the jth spacecraft. Note that the ith filter landmark can have a correlated keypoint in the image from each spacecraft at the current time step but

can only correlate to a single keypoint in each image.

Mahalanobis distance is a measure of the distance between the distribution of a random variable and a sample of that random variable. In this case, the random variable is the difference between the kth keypoint center $\boldsymbol{l}_k$ and the expected pixel measurement $\tilde{\boldsymbol{l}}_i$ of the corresponding landmark based on the filter state estimate. The distribution of this difference is a zero-mean Gaussian distribution with a covariance equal to the sum of the error covariances of $\boldsymbol{l}_k$ and $\tilde{\boldsymbol{l}}_i$. This assumes an unbiased filter estimate and that the pixel measurement error is uncorrelated with the filter state estimate error.

The ACAF position, $\boldsymbol{L}_i$, of the landmark is projected into the image frame using the finite projective camera model [44]

$$\begin{bmatrix} uw \\ vw \\ w \end{bmatrix} = \hat{\mathbf{K}} \underset{ACI \to CF_j}{\mathbf{R}} \begin{bmatrix} \underset{ACAF \to ACI}{\mathbf{R}} & -\boldsymbol{r}_j \end{bmatrix} \begin{bmatrix} \boldsymbol{L}_i \\ 1 \end{bmatrix}. \quad (1)$$

The projected pixel measurements of the landmark center

$$\tilde{\boldsymbol{l}}_i = \begin{bmatrix} u \\ v \end{bmatrix} \quad (2)$$

are computed by dividing the first two elements of Eq. (1) by w, which is the common factor of the homogeneous coordinate of $\tilde{\boldsymbol{l}}_i$. The rotation matrix from the ACI frame to the CF frame of the jth spacecraft is $\underset{ACI \to CF_j}{\mathbf{R}}$, which is provided by the onboard star tracker. The rotation matrix from the ACAF frame to the ACI frame is denoted $\underset{ACAF \to ACI}{\mathbf{R}}$ and is computed from the estimated asteroid rotational parameters. The ACI vector of the jth spacecraft center of mass relative to the asteroid center of mass is $\boldsymbol{r}_j$. Finally, the camera calibration matrix is,

$$\hat{\mathbf{K}} = \begin{bmatrix} \tilde{f}_x & \gamma & c_x \\ 0 & \tilde{f}_y & c_y \\ 0 & 0 & 1 \end{bmatrix}, \quad (3)$$

where $\tilde{f}_x$ and $\tilde{f}_y$ are the camera focal length divided by the pixel pitch in the CF frame x and y directions, respectively. The principal point in pixels is denoted $\boldsymbol{c} = [c_x,\ c_y]^T$. The scalar, γ, is a skew factor generally determined from camera calibration.

The image frame covariance, $\tilde{\mathbf{P}}_{l,i}$, associated with $\tilde{\boldsymbol{l}}_i$ is computed through a linear mapping of the error covariances of the observing spacecraft position and the asteroid rotational parameters contained in the filter state. This linear covariance mapping utilizes the partial derivatives of Eq. (2) with respect to the spacecraft position and asteroid rotational parameters. These partial derivatives are easily derived and are omitted here for brevity.

The Mahalanobis distance m_{ik} between the distribution of $\boldsymbol{l}_k - \tilde{\boldsymbol{l}}_i$ and the sampled value is

$$m_{ik} = \sqrt{\left(\boldsymbol{l}_k - \tilde{\boldsymbol{l}}_i\right)^T \left(\tilde{\mathbf{P}}_{l,i} + \mathbf{R}_k\right)^{-1} \left(\boldsymbol{l}_k - \tilde{\boldsymbol{l}}_i\right)}. \quad (4)$$

Here, $\mathbf{R}_k$ is the measurement error covariance of the kth keypoint pixel center. Any k paired with landmark i that results in an m_{ik} above a threshold are rejected as a match. That threshold, m_t, is determined by

$$m_t = \sqrt{-2\ln(p_m)}, \quad (5)$$

The parameter, p_m, is a tunable probability threshold such that the correlation between landmark i and keypoint k is rejected if the probability of getting a larger Mahalanobis distance than m_{ik} is less than p_m when assuming landmark i and keypoint k are correlated.

Nevertheless, there are typically multiple candidate keypoints with $m_{ik} < m_t$ because interesting asteroid surface points tend to cluster (e.g., keypoints detected on a crater rim or a rocky pile). This means another keypoint right next to the true match might be selected simply because of the noise in landmark and spacecraft state estimation. The feature descriptor, $\boldsymbol{d}_i$, associated with a landmark is retained any time it is correlated in an image. To further eliminate candidate keypoints, the $\boldsymbol{d}_i$ from the previous time step is compared to the feature descriptor, $\boldsymbol{d}_k$, of each candidate keypoint. The feature descriptors are compared by taking the L_2 norm of their difference. A maximum threshold, $\delta_{d,t}$, is also imposed on the feature descriptor differences to eliminate outliers.

The keypoint k^* in the image from the jth spacecraft that correlates to filter landmark i is determined through the weighted optimization problem,

$$\begin{aligned} k^* = \ & \underset{k}{\text{argmin}} && \|\boldsymbol{d}_i - \boldsymbol{d}_k\|_2 + \hat{w} m_{ik} \\ & \text{subject to} && m_{ik} \le m_t \\ & && \|\boldsymbol{d}_i - \boldsymbol{d}_k\|_2 \le \delta_{d,t}. \end{aligned} \quad (6)$$

The Mahalanobis distance tends to be much smaller than the descriptor difference so a weight, $\hat{w}$, is empirically determined to make them comparable. The $\boldsymbol{d}_i$ from spacecraft j is used when available but if not, the $\boldsymbol{d}_i$ of another spacecraft is used. If there are no keypoints that satisfy the constraints in Eq. (6), landmark i is assumed to not correlate to any keypoints in the image. When the k^*th keypoint is correlated to the ith landmark, the keypoint's centroid, $\boldsymbol{l}_{k^*}$, is provided to the estimation filter as the pixel measurement associated with the ith landmark.

This completes the process to correlate keypoint k^* in the image from the jth spacecraft to landmark i. This process is repeated for all spacecraft and landmarks currently in the filter state that are visible to the spacecraft at that time step. Using only visible landmarks for correlation avoids incorrect matches and reduces computation cost. The subset of landmarks visible to the spacecraft is determined by finding the convex hull of the point cloud between the center of the actively tracked landmarks and the spacecraft taking the image [50].

Step Two: Initialize New Landmarks via Stereovision

The second step initializes new landmarks into the filter state by using multi-agent stereovision to reconstruct the ACAF positions of keypoints matched via spacecraft to spacecraft correlation. Spacecraft to spacecraft correlation compares one spacecraft's keypoint descriptors directly to another spacecraft's at the same time step. For each possible pair of spacecraft, the keypoints in the two images are correlated using the descriptor-matching algorithm devised by Lowe in [42]. As a consistency check with the filter landmark correlations determined in the previous subsection via Eq. (6), keypoints that were matched to a filter landmark are not considered.

Each pair of correlated keypoints is reconstructed into the 3D ACAF frame via multi-agent stereovision. The stereovision estimates are calculated using the homogeneous linear

triangulation method from Hartley and Zisserman [44]. This procedure is explained here in the context of landmarks and spacecraft.

Equation (1) can be reduced to a concise form,

$$\boldsymbol{l}_{h,j} = \mathbf{M}_j \boldsymbol{L}_h. \tag{7}$$

Here $\boldsymbol{l}_{h,j} = [uw, vw, w]^T$, $\boldsymbol{L}_h = [\boldsymbol{L}_i^T, 1]^T$, and

$$\mathbf{M}_j = \hat{\mathbf{K}} \underset{ACI \to CF_j}{\mathbf{R}} \begin{bmatrix} \underset{ACAF \to ACI}{\mathbf{R}} & -\boldsymbol{r}_j \end{bmatrix}. \tag{8}$$

is the camera projective transform of the jth spacecraft. Given the matched pixel measurements from two spacecraft, $\boldsymbol{l}_{h,1} = [u_1, v_1, 1]^T$ and $\boldsymbol{l}_{h,2} = [u_2, v_2, 1]^T$, and their respective projective transforms, $\mathbf{M}_1$ and $\mathbf{M}_2$, two equations can be formed from Eq. (7):

$$\boldsymbol{l}_{h,1} = \mathbf{M}_1 \boldsymbol{L}_h \tag{9}$$

$$\boldsymbol{l}_{h,2} = \mathbf{M}_2 \boldsymbol{L}_h. \tag{10}$$

Because the cross product of two parallel vectors is zero, two more equations can be formed,

$$\boldsymbol{l}_{h,1} \times \mathbf{M}_1 \boldsymbol{L}_h = \mathbf{0} \tag{11}$$

$$\boldsymbol{l}_{h,2} \times \mathbf{M}_2 \boldsymbol{L}_h = \mathbf{0}. \tag{12}$$

Equations (9 - 12) share the same 3D landmark position and can be combined into a form, $\mathbf{A}\boldsymbol{L}_h = \mathbf{0}$, where

$$\mathbf{A} = \begin{bmatrix} u_1 \boldsymbol{M}_1^{3T} - \boldsymbol{M}_1^{1T} \\ v_1 \boldsymbol{M}_1^{3T} - \boldsymbol{M}_1^{2T} \\ u_2 \boldsymbol{M}_2^{3T} - \boldsymbol{M}_2^{1T} \\ v_2 \boldsymbol{M}_2^{3T} - \boldsymbol{M}_2^{2T} \end{bmatrix}. \tag{13}$$

Each $\boldsymbol{M}_j^{aT}$ is the is the ath row of $\mathbf{M}_j$. There is likely no exact solution to $\mathbf{A}\boldsymbol{L}_h = 0$ because there is noise in both $\boldsymbol{l}_{h,j}$ and $\mathbf{M}_j$. Instead, $\boldsymbol{L}_h$ is considered the minimizer of $\|\mathbf{A}\boldsymbol{L}_h\|_2$ subject to $\|\boldsymbol{L}_h\|_2 = 1$. The constraint is included because $\boldsymbol{L}_h = \mathbf{0}$ is a trivial solution. The matrix $\mathbf{M}_j$ is only defined up to a scale, so the value of $\|\boldsymbol{L}_h\|_2$ is unimportant. This optimization problem is solved via singular value decomposition where $\boldsymbol{L}_h$ is the unit right-singular vector corresponding to the smallest singular value of $\mathbf{A}$. The final $\boldsymbol{L}_i$ is recovered by dividing the first three elements of $\boldsymbol{L}_h$ by its fourth element.

The covariance of each new stereovision estimate $\boldsymbol{L}_i$ and its cross covariances with the other filter state parameters are computed through a linear mapping of the covariance of the vector concatenation of the observing spacecraft positions and the asteroid rotation parameters as provided by the estimation filter output. The linear covariance mapping uses the partial derivatives of the stereovision estimates with respect to the observing spacecraft positions and the asteroid rotational parameters. These partial derivatives are approximated through central finite differencing.

It is important to note the competing camera angular separation requirements between Lowe's descriptor-matching algorithm and stereovision. In [37], keypoint correlation including Lowe's algorithm was shown to decrease as spacecraft separation increased even though the same landmarks remained within the field of view, most likely because the perspective may have changed too much to directly compare the feature descriptors. On the other hand, [51] and [52] both showed that uncertainty in stereovision estimates decreases as camera angular separation increases. The stereovision process essentially finds the closest point of intersection between the rays projected by the two image points into the 3D frame. If the origins of the rays (i.e., camera locations) are close together, the rays can become nearly parallel and, thus, the true intersection is more uncertain [51]. The intersatellite separation must be small enough for accurate spacecraft to spacecraft correlation but large enough for accurate stereovision.

Each correlation pair and associated ACAF position and covariance estimate undergo two more checks before being added to the filter state. First, if the L_2 norm of the diagonal of the 3-by-3 ACAF covariance of an estimate is greater than $P_{L,max}$, the estimate and it's keypoint correlation pair is discarded. Second, if a keypoint from one spacecraft was correlated to a keypoint from two or more spacecraft, there will be an ACAF estimate for each match pair. Only the estimate that has the smallest maximum eigenvalue of the ACAF error covariance is kept.

Once these checks are passed, step two is complete. The ACAF landmark state estimates and their associated covariances for keypoint pairs that did not match any filter landmarks are added to the filter state. Their pixel measurements are not used for the filter update in this time step because they were already used to compute the new landmark estimates.

Step Three: Landmark Retirement

Filter landmarks have been correlated to specific keypoints in images and new landmarks have been reconstructed from their keypoint pairs in the ACAF frame to add to the filter. This leaves the final step of the landmark tracking and stereovison subsystem: determine which landmarks to retire from the filter state and how to maintain the landmark database. Retired landmarks are retained in the database for use in global shape reconstruction only. They are never used for any correlation method again, nor are their ACAF positions and covariances updated.

Landmarks are retired because true correlations may not pass the descriptor difference constraint in Eq. (6) of landmark tracking if too much time has passed from the last time it was seen. The same landmarks could end up being initialized into the filter multiple times and confuse correlation or lead to cumbersome computation times because of an ever growing filter state. When a landmark has not been correlated in n_r steps, that landmark is retired. That is, it is removed from the filter state, added to the retired database, and is no longer tracked. The user-specified parameter, n_r, can be determined from orbit conditions and the keypoint descriptor method as specified in [37].

As landmarks are retired from the filter state, it is beneficial to remove some landmarks from the database in order to avoid excessive memory requirements. Landmarks should be removed in a way to avoid storing duplicate landmarks and to cover the asteroid surface as uniformly as possible to best capture the shape for global shape reconstruction. Thus, when a landmark is retired, all existing retired landmarks within Euclidean distance, d_r, of the newly retired landmark's position are found. Then, one-by-one, the newly retired landmark and the existing retired landmarks are compared to see if their covariances overlap significantly via

$$l_o = \sqrt{\lambda_*} + \sqrt{\lambda_r} - d_{*,r}. \tag{14}$$

Here, λ_* and λ_r are the maximum eigenvalues of the newly retired landmark and the existing retired landmark covariance, respectively. The Euclidean distance between the two landmarks is $d_{*,r}$. If $l_o < 0$, the landmark with the smaller maximum covariance eigenvalue is retained in the database, and the other landmark is deleted. When a landmark is retired from the filter state that has not been correlated to an image keypoint after its stereovision initialization, it is deleted from the landmark database. Such landmarks often have relatively large uncertainties and may be the result of an incorrect correlation of two image keypoints.

Finally, the work of the landmark tracking and stereovision subsystem is complete. Step one correlates filter landmarks to the images and returns their pixel measurements via filter to spacecraft correlation. Step two initializes new landmarks into the filter via multi-agent stereovision and spacecraft to spacecraft correlation. Step three retires landmarks from the filter state and maintains a database of retired landmarks for later use.

4. STATE ESTIMATION FILTER

The estimation filter fuses the pixel measurements from the landmark tracking and stereovision subsystem with the inter-satellite RF measurements to estimate the spacecraft states and asteroid characteristics. A UKF [11, 53] is utilized because it is more accurate for nonlinear systems than an extended Kalman filter and is more computationally efficient than particle filtering techniques [11]. Thus, a UKF provides a good balance between computational cost and accuracy for this application. The ANS UKF computation time is significantly reduced with no loss of accuracy through the recently developed exploiting triangular structure technique [10]. The filter is made robust to system nonlinearities and dynamics modeling deficiencies through measurement underweighting and adaptive estimation of the process noise covariance. The state estimation filter is executed entirely on the mothership (see Figure 2).

The estimated filter state is

$$\boldsymbol{x} = [\boldsymbol{\psi}^T \ \boldsymbol{G}^T \ \boldsymbol{x}_1^T \ C_{r,1} \ \ldots \ \boldsymbol{x}_{n_s}^T \ C_{r,n_s} \ \boldsymbol{\delta b}^T \ \boldsymbol{L}_1^T \ \ldots \ \boldsymbol{L}_{n_l}^T]^T \tag{15}$$

where n_s is the number of spacecraft and n_l is the number of landmark states currently in the filter state. Here $\boldsymbol{\psi} = [\alpha \ \delta \ \omega]^T$ parameterizes the rotational motion of the asteroid where α and δ are the right ascension and declination of the asteroid spin axis respectively with respect to the ACI frame, and ω is the asteroid spin rate [54]. The current filter implementation assumes the asteroid rotates uniformly about its maximum moment of inertia principle axis, which is true for the majority of asteroids [55, 56]. The vector $\boldsymbol{G}$ contains the asteroid gravitational parameter as well as the normalized spherical harmonic coefficients of the asteroid gravity field where the normalization factor is [57]

$$\kappa_{nm} = \sqrt{\frac{(n+m)!}{(2-\delta_{0m})(2n+1)(n-m)!}} \tag{16}$$

Here, n and m are the degree and order of the gravity coefficient respectively, and δ_{ij} is the Kronecker delta function. The inertial Cartesian state and solar radiation pressure coefficient respectively of the ith spacecraft are $\boldsymbol{x}_i$ and $C_{r,i}$. The clock offset and drift of each deputy with respect to the mothership multiplied by the speed of light are contained in $\boldsymbol{\delta b}$. The ACAF 3D position vector of the ith tracked landmark is $\boldsymbol{L}_i$.

Before each measurement update, stereovision estimates of new landmark 3D ACAF positions are added to the filter state. The covariances of the stereovision estimates and their cross covariances with each other and the rest of the filter state parameters are incorporated in the filter error covariance. Since SIFT features are not robust to large changes in perspective and illumination conditions, landmarks in the filter state that have not been observed by any spacecraft for a specified amount of time are removed from the filter state. An initial mean state estimate and error covariance of the state in Eq. (15), except for landmark states, is provided by the brief ground-in-the-loop initialization phase.

Dynamics Modeling

Each UKF call consists of a time update and a measurement update. In both the time and measurement updates, $2n+1$ sigma points are deterministically generated where n is the current number of state variables. In the time update, each sigma point is propagated over the measurement interval. Except for the spacecraft states and $\boldsymbol{\delta b}$, all the state variables are treated as constants, and their dynamics are modeled as identity. The spacecraft states are propagated through a fourth-order Runge-Kutta numerical integration where the modeled spacecraft accelerations take into account the spherical harmonic gravity coefficients of the asteroid up to a specified degree and order, solar radiation pressure with a constant spacecraft surface area, and third body gravity from the sun.

Although there are various ways to model the many sources of noise that alter the frequency of an oscillator over time, it is common to model an atomic clock as a two state system [58]. The clock states of the ith spacecraft are

$$\boldsymbol{\eta}_i(t) = \begin{bmatrix} \eta_i(t) \\ \dot{\eta}_i(t) \end{bmatrix} \tag{17}$$

where $i = 1$ corresponds to the mothership. The clock offset, which is the difference between the clock time and the true time, is denoted $\eta_i(t)$. The clock drift is $\dot{\eta}_i(t) = \frac{d}{dt}\eta_i(t)$. The dynamical model of the clock states is

$$\dot{\boldsymbol{\eta}}_i(t) = \begin{bmatrix} 0 & 1 \\ 0 & 0 \end{bmatrix} \boldsymbol{\eta}_i(t) + \boldsymbol{\epsilon}_{\eta i}(t) \tag{18}$$

where $\boldsymbol{\epsilon}_{\eta i}(t) \in \mathbb{R}^2$ is a zero-mean white Gaussian process with the power spectral density

$$\widetilde{\mathbf{Q}}_{\eta i} = \begin{bmatrix} q_{1_i} & 0 \\ 0 & q_{2_i} \end{bmatrix} \tag{19}$$

The values of q_1 and q_2 for a specific clock can be estimated by fitting the equation [59]

$$\sigma_y^2(\tau) = \frac{q_1}{\tau} + \frac{q_2 \tau}{3} \tag{20}$$

to empirically determined values of the Allan variance $\sigma_y^2(\tau)$ where τ is the averaging interval.

The discrete-time solution to Eq. (18) is

$$\boldsymbol{\eta}_i(t_k) = \boldsymbol{\Phi}_\eta(t_k, t_{k-1})\boldsymbol{\eta}_i(t_{k-1}) + \boldsymbol{w}_{\eta i}(t_k) \tag{21}$$

where

$$\boldsymbol{\Phi}_\eta(t_k, t_{k-1}) = \begin{bmatrix} 1 & \Delta t_k \\ 0 & 1 \end{bmatrix} \tag{22}$$

and $\Delta t_k = t_k - t_{k-1}$. It is easily shown that the discrete-time process noise $\boldsymbol{w}_{\eta i}(t_k)$ is uncorrelated in time, zero-mean, and normally distributed with covariance [58]

$$\mathbf{Q}_{\eta_i}(t_k) = \begin{bmatrix} q_{1_i}\Delta t_k + q_{2_i}\frac{\Delta t_k^3}{3} & q_{2_i}\frac{\Delta t_k^2}{2} \\ q_{2_i}\frac{\Delta t_k^2}{2} & q_{2_i}\Delta t_k \end{bmatrix} \tag{23}$$

The biases of the RF measurements are

$$\boldsymbol{\delta b}_i(t) = \begin{bmatrix} \delta b_i(t) \\ \dot{\delta} b_i(t) \end{bmatrix} = c \begin{bmatrix} \eta_i(t) - \eta_1(t) \\ \dot{\eta}_i(t) - \dot{\eta}_1(t) \end{bmatrix} \tag{24}$$

where c is the speed of light. Note that $\boldsymbol{\delta b}_1 = \mathbf{0}$ by definition. Light time delay is neglected in Eq. (24) because $E[\eta_i(t+\tau)] - \eta_i(t)] = \tau E[\dot{\eta}_i(t)]$ and $\text{Var}(\eta_i(t+\tau) - \eta_i(t)) = q_{1_i}\tau + q_{2_i}\frac{\tau^3}{3}$ are small. The dynamics of $\boldsymbol{\delta b}_i(t)$ are described by

$$\boldsymbol{\delta b}_i(t_k) = \boldsymbol{\Phi}_\eta(t_k, t_{k-1})\boldsymbol{\delta b}_i(t_{k-1}) + \boldsymbol{w}_{\delta bi}(t_k) \tag{25}$$

where

$$\boldsymbol{w}_{\delta bi}(t_k) = c(\boldsymbol{w}_{\eta i}(t_k) - \boldsymbol{w}_{\eta 1}(t_k)) \tag{26}$$

The vector

$$\boldsymbol{\delta b}(t_k) = [\boldsymbol{\delta b}_2(t_k)^T \dots \boldsymbol{\delta b}_{n_s}(t_k)^T]^T \tag{27}$$

is estimated as part of the filter state (see Eq. (15)). The associated discrete-time process noise of $\boldsymbol{\delta b}(t_k)$ is

$$\boldsymbol{w}_{\delta b}(t_k) = [\boldsymbol{w}_{\delta b_2}(t_k)^T \dots \boldsymbol{w}_{\delta b_{n_s}}(t_k)^T]^T \tag{28}$$

The random vector $\boldsymbol{w}_{\delta b}(t_k)$ is normally distributed and uncorrelated in time with covariance

$$\mathbf{Q}_{\delta b}(t_k) = \text{E}[\boldsymbol{w}_{\delta b}(t_k)\boldsymbol{w}_{\delta b}(t_k)^T] \tag{29}$$

$$= \begin{bmatrix} \mathbf{Q}_{\delta b_{2,2}}(t_k) & \mathbf{Q}_{\delta b_{2,3}}(t_k) & \dots & \mathbf{Q}_{\delta b_{2,n_s}}(t_k) \\ \mathbf{Q}_{\delta b_{3,2}}(t_k) & \mathbf{Q}_{\delta b_{3,3}}(t_k) & \dots & \mathbf{Q}_{\delta b_{3,n_s}}(t_k) \\ \vdots & \vdots & \ddots & \vdots \\ \mathbf{Q}_{\delta b_{n_s,2}}(t_k) & \mathbf{Q}_{\delta b_{n_s,3}}(t_k) & \dots & \mathbf{Q}_{\delta b_{n_s,n_s}}(t_k) \end{bmatrix} \tag{30}$$

Assuming the noises of different clocks are uncorrelated,

$$\mathbf{Q}_{\delta b_{i,j}}(t_k) = \text{E}[\boldsymbol{w}_{\delta bi}(t_k)\boldsymbol{w}_{\delta bj}(t_k)^T] \tag{31}$$

$$= \begin{cases} c^2(\mathbf{Q}_{\eta_i}(t_k) + \mathbf{Q}_{\eta_1}(t_k)) & \text{for } i = j \\ c^2\mathbf{Q}_{\eta_1}(t_k) & \text{otherwise} \end{cases} \tag{32}$$

Measurement Modeling

In the measurement update, the predicted measurements for each sigma point are computed. The one-way RF pseudorange measurements between each pair of spacecraft at the epoch t_k are modeled as

$$\rho_{ij}(t_k) = ||\boldsymbol{\rho}_{ij}(t_k)|| + \delta b_j - \delta b_i \tag{33}$$

The transmitting and receiving satellites are indicated by the subscripts i and j respectively. The vector from the ith spacecraft antenna to that of the jth spacecraft is $\boldsymbol{\rho}_{ij}$. The intersatellite one-way Doppler measurements are modeled as

$$\dot{\rho}_{ij}(t_k) = \dot{\boldsymbol{\rho}}_{ij}(t_k) \cdot \frac{\boldsymbol{\rho}_{ij}(t_k)}{||\boldsymbol{\rho}_{ij}(t_k)||} + \dot{\delta} b_j - \dot{\delta} b_i \tag{34}$$

Note that $\delta b_1 = \dot{\delta} b_1 = 0$ by definition because the biases are defined relative to the mothership clock. The motion of the spacecraft during the signal time of flight is neglected in Eqs. (33) and (34) because the resulting errors are much smaller than the measurement noise for the considered relative spacecraft motion.

The pixel measurements, u and v, of the ith tracked landmark taken by a camera onboard the jth spacecraft are given by the pin-hole camera model in Eqs. (1-2). The correspondences between detected 2D image keypoints and landmarks in the filter state are provided by the landmark tracking and stereovision subsystem described in Section 3.

Computationally Efficient and Robust Estimation

In the time update, each sigma point is propagated over the measurement interval using the filter modeled dynamics [11]. A traditional UKF would require $(2n+1)n_s$ orbit propagations for each time update where n is the number of state variables and n_s is the number of spacecraft. These orbit propagations dominate the total UKF runtime. However, the runtime of the ANS UKF is significantly reduced with no loss of accuracy through the recently developed exploiting triangular structure technique [10]. Each sigma point is a different realization of the state vector in Eq. (15). The first sigma point is the mean state estimate and the other sigma points are the mean state estimate plus or minus a scaled column of the matrix square root of the filter error covariance [11]. Due to the lower triangular structure of the Cholesky decomposition matrix square root, many sigma points will have orbit propagations that are identical to the first sigma point orbit propagations. The state ordering in Eq. (15) is specifically chosen to minimize the number of unique orbit propagations such that the orbit propagations for the first sigma point can be reused for other sigma points as much as possible. This reduces the number of required orbit propagations from $(2n+1)n_s$ to $2n_s(1/2 + \dim(\boldsymbol{\psi}) + \dim(\boldsymbol{G})) + 2\sum_{i=0}^{n_s-1} 7(n_s - i)$ where $\dim(\cdot)$ denotes the cardinality of a vector (e.g., $\dim(\boldsymbol{\psi}) = 3$). Although the exploiting triangular structure technique can also be used to reduce the computation time of the measurement update, it is not used here because the filter computation time is dominated so heavily by the time update.

The performance of a Kalman filter can degrade considerably if there are large, neglected higher order effects. In cases where the state uncertainty is large relative to that of the measurement uncertainty, neglecting significant higher order effects of the nonlinear measurement models can result in a theoretical state error covariance that decreases more quickly than the true state errors, resulting in filter inconsistency [60]. This phenomenon is especially of concern before filter convergence when the state uncertainty is relatively large. To overcome this obstacle, various measurement underweighting schemes have been proposed to increase the innovation covariance in order to slow the convergence of the filter error covariance. Zanetti gives a comprehensive review of measurement underweighting techniques [60]. Here, Lear's underweighting method is employed during filter convergence because it is simple and treats the second order effects as a scaling of the first order effects, which adapts the inflation

of the innovation covariance according to the size of the state error covariance [60].

The performance of a Kalman filter is also heavily dependent on the accuracy of the modeled process and measurement noise covariances. Poor modeling of these covariances can lead to filter inconsistency and divergence. Modeling the process noise covariance is especially challenging for an asteroid mission because the dynamical environment is poorly known a priori and the process noise statistics can change dramatically as the spacecraft orbits change throughout the mission. In order to make the estimation filter robust to dynamics modeling deficiencies, the recently developed adaptive state noise compensation algorithm is used to efficiently estimate the process noise covariance of the spacecraft states online [49]. This technique models the process noise covariance of each Cartesian spacecraft state at the kth time step as

$$\mathbf{Q}_k = \begin{bmatrix} \frac{1}{3}\Delta t_k^3 \widetilde{\mathbf{Q}}_k & \frac{1}{2}\Delta t_k^2 \widetilde{\mathbf{Q}}_k \\ \frac{1}{2}\Delta t_k^2 \widetilde{\mathbf{Q}}_k & \Delta t_k \widetilde{\mathbf{Q}}_k \end{bmatrix}, \tag{35}$$

where $\Delta t_k = t_k - t_{k-1}$. The power spectral density of the unmodeled spacecraft accelerations, $\widetilde{\mathbf{Q}} \in \mathbb{R}^{3\times 3}$, is assumed diagonal and is adaptively tuned after each filter call. Estimating $\widetilde{\mathbf{Q}}$ is very computationally efficient and can easily incorporate lower and upper bounds on each diagonal element. Each lower bound must be at least zero to ensure $\mathbf{Q}_k$ is positive semi-definite.

A coarse upper bound is derived here based on the largest expected unmodeled acceleration the spacecraft will experience, a_{max}. Over a small time interval Δt_k, the greatest amount by which the velocity in any axis is changed due to a_{max} is $a_{max}\Delta t_k$. Assuming that $a_{max}\Delta t_k$ is greater than the change in velocity that will be caused by unmodeled accelerations, $a_{max}\Delta t_k$ is set equal to the square root of an element on the main diagonal of the velocity covariance portion of Eq. (35) to yield the upper bound

$$\widetilde{Q}_u = a_{max}^2 \Delta t \tag{36}$$

Selection of a_{max} should be based on the modeled dynamics and the best knowledge of the true dynamics. One conservative option is to select a_{max} as the maximum acceleration a spacecraft would experience in its orbit due to the spherical harmonic gravity coefficient J_2, which is

$$a_{max} = \frac{3\mu J_2 R_{ref}^2}{2r^4} \tag{37}$$

Here μ and R_{ref} are the gravitational parameter and reference radius respectively of the central body. The distance of the spacecraft from the central body center of mass is r. The value of a_{max} is estimated using the current best knowledge of μ, J_2, and r. Eq. (36) can also be used as an initial guess of $\widetilde{\mathbf{Q}}$.

5. GLOBAL SHAPE RECONSTRUCTION

A global asteroid shape model is integral to many mission operations. It helps keep the spacecraft at a safe distance from the asteroid. It also enables the use of a polyhedral gravity model, which is important for operations inside the smallest circumscribing sphere (i.e., Brillouin sphere) of the asteroid where a spherical harmonic gravity model may diverge [39]. A spherical harmonic shape model is particularly powerful because it can be paired with a spherical harmonic gravity model to infer characteristics of the body mass distribution [38]. This section describes a novel technique to generate a global spherical harmonic shape model from a 3D point cloud of estimated surface landmark positions. The global shape model is obtained through a regularized least squares fit of the spherical harmonic coefficients to the estimated 3D landmark positions, weighting each landmark according to its uncertainty. A new regularization procedure leveraging generalized cross validation and a priori knowledge of the shape characteristics of celestial bodies is developed to prevent over fitting, thus providing accurate surface reconstruction between landmark point estimates. In ANS, this technique can be used periodically to generate a global asteroid 3D shape model based on the landmark point estimates in the landmark database provided by the subsystems discussed in Sections 3 and 4. Global shape reconstruction is executed entirely on the mothership (see Figure 2).

Any surface whose radial distance is a square-integrable function of latitude λ and longitude ϕ can be represented through a spherical harmonic expansion [38]

$$r(\lambda,\phi) = \sum_{n=0}^{N}\sum_{m=0}^{n} (\bar{A}_{nm}\cos m\lambda + \bar{B}_{nm}\sin m\lambda)\bar{P}_{nm}(\sin\phi) \tag{38}$$

where $r(\lambda,\phi)$ is the distance of the surface from the origin. As $N \to \infty$, Eq. (38) describes the surface exactly. In practice, Eq. (38) is truncated to some finite maximum degree N. The spherical harmonics coefficients A_{nm} and B_{nm} of degree n and order m are normalized such that $\bar{A}_{nm} = \kappa_{nm}A_{nm}$ and $\bar{B}_{nm} = \kappa_{nm}B_{nm}$, where κ_{nm} is defined in Eq. (16). The associated Legendre functions $P_{nm}(u)$ are also normalized such that $\bar{P}_{nm}(u) = \kappa_{nm}^{-1}P_{nm}(u)$. For a set of n_l 3D surface points, Eq. (38) can be written in matrix form as

$$\boldsymbol{r} = \mathbf{A}\boldsymbol{s} \tag{39}$$

Here,

$$\boldsymbol{r} = [r_1 \ \ldots \ r_{n_l}]^T \tag{40}$$

is the concatenation of the Eulidean norm of each landmark position vector,

$$\boldsymbol{s} = [\bar{A}_{00}\ \bar{A}_{10}\ \ldots\ \bar{A}_{NN}\bar{B}_{11}\ \bar{B}_{21}\ \ldots\ \bar{B}_{NN}]^T \tag{41}$$

is a vector containing the normalized spherical harmonic shape coefficients up through degree and order N, and

$$\mathbf{A} = \begin{bmatrix} \bar{P}_{00}(\sin\phi_1) & \ldots & \bar{P}_{NN}(\sin\phi_1)\sin N\lambda_1 \\ \vdots & \ddots & \vdots \\ \bar{P}_{00}(\sin\phi_{n_l}) & \ldots & \bar{P}_{NN}(\sin\phi_{n_l})\sin N\lambda_{n_l} \end{bmatrix} \tag{42}$$

is defined such that Eq. (38) is satisfied for each r_i.

Given a set of 3D positions on the surface of an object, spherical harmonic coefficients up to a specified degree and order representing the surface can be obtained through the least squares minimization

$$\arg\min_{\boldsymbol{s}} ||\mathbf{A}\boldsymbol{s} - \boldsymbol{r}||^2 \tag{43}$$

Unfortunately, the solution of Eq. (43) often results in over fitting, which leads to large surface protrusions in areas with few landmarks [61,62]. Over fitting is especially pronounced

as the degree of the spherical harmonics expansion increases. To prevent over fitting for weighted least squares problems in general, regularization is often used. One of the most common regularization approaches is referred to as Tikhonov regularization or ridge regression [63, 64].

Regularization

We take a novel approach to prevent over fitting by leveraging a priori knowledge of the shape characteristics of celestial bodies. The root mean square (RMS) power spectrum of the shape spherical harmonic coefficients of a body is defined for each degree n as

$$\sigma_{sh}(n) = \left(\frac{1}{2n+1} \sum_{m=0}^{n} (\bar{A}_{nm}^2 + \bar{B}_{nm}^2) \right)^{1/2}, \tag{44}$$

which is rotation invariant [38]. Kaula empirically showed that the RMS power spectra of the gravity spherical harmonic coefficients of terrestrial bodies tend to follow a power law [65, 66], decreasing as $1/n^2$. Similarly, many authors have observed that $\sigma_{sh}(n)$ is also well described by a power law [38, 67]

$$\sigma_{sh}(n) = \frac{K}{n^\alpha} \tag{45}$$

for terrestrial and minor bodies. The constants K and α have been empirically determined for various bodies such as Venus [68, 69], Mars [69], and Phobos [70]. For the Earth, the Vening Meinesz rule [67, 71] defines $\alpha = 2$, although authors with more accurate, modern data estimate $\alpha = 1.8$ [69, 72]. Recently, Ermakov et al. [67] analyzed the data from numerous space missions to various bodies in the solar system and found that $\alpha = 1.67$ and $\alpha = 1.88$ provide a good fit for terrestrial and minor bodies respectively.

This a priori information can be incorporated in the least squares optimization through a Tikhonov regularization term. Additionally taking into account the uncertainty of the estimated landmark positions results in the optimization

$$\arg\min_{\boldsymbol{s}} \frac{1}{n_l} ||\mathbf{P}^{-1/2}(\mathbf{A}\boldsymbol{s} - \boldsymbol{r})||^2 + \nu ||\mathbf{\Gamma}^{1/2}\boldsymbol{s}||^2 \tag{46}$$

Here $\nu \geq 0$ is a weighting factor, $\mathbf{P}$ is the error covariance of $\boldsymbol{r}$, and the matrix square root of $\mathbf{P}$ is denoted $\mathbf{P}^{1/2}$. Leveraging the power rule in Eq. (45), the Tikhonov matrix is defined as the diagonal matrix

$$\mathbf{\Gamma}^{1/2} = \begin{bmatrix} \deg(s_1)^\alpha + \epsilon & 0 & \dots & 0 \\ 0 & \deg(s_2)^\alpha & \dots & 0 \\ \vdots & \vdots & \ddots & \vdots \\ 0 & 0 & \dots & \deg(s_{n_s})^\alpha \end{bmatrix} \tag{47}$$

$$= \begin{bmatrix} \epsilon & 0 & \dots & 0 \\ 0 & 1 & \dots & 0 \\ \vdots & \vdots & \ddots & \vdots \\ 0 & 0 & \dots & N^\alpha \end{bmatrix} \tag{48}$$

where $\deg(s_i)$ is the degree of the ith element of $\boldsymbol{s}$, and n_s is the cardinality of $\boldsymbol{s}$. An arbitrarily small number ϵ is added to the element in the first row and column of $\mathbf{\Gamma}^{1/2}$ in order for $\mathbf{\Gamma}^{1/2}$ to be invertible, which is required later to determine ν. The structure of $\mathbf{\Gamma}^{1/2}$ encourages surface smoothness similar to other celestial bodies by penalizing large values for large degree coefficients. The Bayesian interpretation of Eq. (46) is that the estimate of the shape coefficients is improved by incorporating the a priori belief that the coefficients are normally distributed with a mean of zero and a covariance of $\nu\mathbf{\Gamma}^{-1}$. Note that $\mathbf{\Gamma}^{-1}$ follows the power law in Eq. (45). It is recommended to follow the work of Ermakov et al. [67] and use $\alpha = 1.67$ for terrestrial bodies and $\alpha = 1.88$ for minor bodies if no other a priori knowledge of α is available.

The error covariance $\mathbf{P}$ can be approximated through the linear mapping

$$\mathbf{P} = \frac{\partial \boldsymbol{r}}{\partial \boldsymbol{x}_L} \mathbf{P}_L \frac{\partial \boldsymbol{r}}{\partial \boldsymbol{x}_L}^T \tag{49}$$

where $\boldsymbol{x}_L = [\boldsymbol{L}_1^T \dots \boldsymbol{L}_{n_l}]^T$ is the vector concatenation of the estimated 3D ACAF landmark positions, and $\mathbf{P}_L$ is the associated error covariance. The partial derivatives in Eq. (49) are

$$\frac{\partial \boldsymbol{r}}{\partial \boldsymbol{x}_L} = \begin{bmatrix} \frac{\partial r_1}{\partial \boldsymbol{L_1}} & \mathbf{0}_{1\times 3} & \dots & \mathbf{0}_{1\times 3} \\ \mathbf{0}_{1\times 3} & \frac{\partial r_2}{\partial \boldsymbol{L_2}} & \dots & \mathbf{0}_{1\times 3} \\ \vdots & \vdots & \ddots & \vdots \\ \mathbf{0}_{1\times 3} & \mathbf{0}_{1\times 3} & \dots & \frac{\partial r_{n_l}}{\partial \boldsymbol{L_{n_l}}} \end{bmatrix} \tag{50}$$

where

$$\frac{\partial r_i}{\partial \boldsymbol{L}_i} = \frac{\boldsymbol{L}_i^T}{||\boldsymbol{L}_i||} \tag{51}$$

The well known solution of Eq. (46) is

$$\hat{\boldsymbol{s}} = (\mathbf{A}^T\mathbf{P}^{-1}\mathbf{A} + n_l\nu\mathbf{\Gamma})^{-1}\mathbf{A}^T\mathbf{P}^{-1}\boldsymbol{r} \tag{52}$$

Selecting the Regularization Weighting Factor

The weighting factor ν determines the importance of surface smoothness relative to fitting the data. A variety of methods have been developed to determine the best value of ν such as the L-curve method [73, 74], Morozov's discrepancy principle [75], minimum χ^2 and equivalent degrees of freedom [76], k-fold cross-validation [77], and Allen's predicted residual error sum of squares (PRESS). The PRESS estimate minimizes the average square error of each data point and the corresponding model predicted value when that point is omitted from the regularized least squares solution [64]. The generalized cross validation (GCV) estimate is a rotation invariant version of Allen's PRESS estimate [64]. Thompson et al. [76] compare several of these methods and found GCV to generally perform well. Since the GCV estimate tends to work well in practice, it is utilized in this paper [78]. To find the GCV optimal ν, Eq. (46) is first transformed to the standard form

$$\arg\min_{\boldsymbol{s}} \frac{1}{n_l} ||\bar{\mathbf{A}}\bar{\boldsymbol{s}} - \bar{\boldsymbol{r}}||^2 + \bar{\nu}||\bar{\boldsymbol{s}}||^2 \tag{53}$$

using the relations

$$\begin{aligned} \bar{\mathbf{A}} &= \mathbf{P}^{-1/2}\mathbf{A}\mathbf{\Gamma}^{-1/2}, & \bar{\boldsymbol{s}} &= \mathbf{\Gamma}^{1/2}\boldsymbol{s} \\ \bar{\boldsymbol{r}} &= \mathbf{P}^{-1/2}\boldsymbol{r}, & \bar{\nu} &= \frac{1}{n_l}\nu \end{aligned} \tag{54}$$

Then the GCV optimal $\bar{\nu}$ is the minimizer of the scalar function

$$V(\bar{\nu}) = \frac{n_l ||\mathbf{B}\bar{r}||^2}{\mathrm{Tr}(\mathbf{B})^2} \tag{55}$$

where $\mathrm{Tr}(\cdot)$ denotes the trace of a matrix, and $\mathbf{B} = \mathbf{I} - \bar{\mathbf{A}}(\bar{\mathbf{A}}^T\bar{\mathbf{A}}+n_l\bar{\nu}\mathbf{I})^{-1}\bar{\mathbf{A}}^T$. The computation of $V(\bar{\nu})$ for various $\bar{\nu}$ can be reduced from $O(n_s^3)$ to $O(n_s)$ after computing some initial $O(n_s^3)$ matrix decompositions [79]. The denominator of $V(\bar{\nu})$ can also be efficiently and accurately approximated for large scale problems using statistical methods [80].

Most often, $V(\bar{\nu})$ has a single well-defined minimum. However, there can be multiple minima [81]. The algorithm proposed by Kent and Mohammadzadeh is recommended because it is guaranteed to find the global minimizer of $V(\bar{\nu})$ [79]. For simplicity in this paper, the optimal $\bar{\nu}$ is found through a three step process. First, an initial bracket on $\bar{\nu}$ is defined using the range of numerically meaningful values derived by Golub and von Matt [80]. Second, a grid search is performed in log space. Third, the $\bar{\nu}$ from the grid search that resulted in the smallest $V(\bar{\nu})$ is refined using the Newton-Rhapson method on the first derivative of $V(\bar{\nu})$. The optimal $\bar{\nu}$ is then used to compute ν through Eq. (53), which is then used to estimate the shape spherical harmonic coefficients through Eq. (52). The first and second derivatives of $V(\bar{\nu})$, which are required for the Newton-Rhapson method, are

$$V'(\bar{\nu}) = \frac{n_l}{\mathrm{Tr}(\mathbf{B})^2}\bar{\boldsymbol{r}}^T(\mathbf{B}^T\mathbf{B}' + \mathbf{B}'^T\mathbf{B})\bar{\boldsymbol{r}} - \frac{2n_l\,\mathrm{Tr}(\mathbf{B}')}{\mathrm{Tr}(\mathbf{B})^3}\bar{\boldsymbol{r}}^T\mathbf{B}^T\mathbf{B}\bar{\boldsymbol{r}} \tag{56}$$

and

$$V''(\bar{\nu}) = \frac{n_l}{\mathrm{Tr}(\mathbf{B})^2}\bar{\boldsymbol{r}}^T(2\mathbf{B}'^T\mathbf{B}' + \mathbf{B}^T\mathbf{B}'' + \mathbf{B}''^T\mathbf{B})\bar{\boldsymbol{r}} - 4\frac{n_l\,\mathrm{Tr}(\mathbf{B}')}{\mathrm{Tr}(\mathbf{B})^3}\bar{\boldsymbol{r}}^T(\mathbf{B}^T\mathbf{B}' + \mathbf{B}'^T\mathbf{B})\bar{\boldsymbol{r}} - 2n_l\bar{\boldsymbol{r}}^T\mathbf{B}^T\mathbf{B}\bar{\boldsymbol{r}}\left(\frac{\mathrm{Tr}(\mathbf{B}'')}{\mathrm{Tr}(\mathbf{B})^3} - \frac{3\,\mathrm{Tr}(\mathbf{B}')^2}{\mathrm{Tr}(\mathbf{B})^4}\right) \tag{57}$$

where $'$ indicates differentiation with respect to $\bar{\nu}$. Equations (56) and (57) are used to verify that the obtained $\bar{\nu}$ corresponds to a local minimum. The derivatives of $\mathbf{B}$ are

$$\mathbf{B}' = n_l\bar{\mathbf{A}}(\bar{\mathbf{A}}^T\bar{\mathbf{A}} + n_l\bar{\nu}\mathbf{I})^{-2}\bar{\mathbf{A}}^T \tag{58}$$

$$\mathbf{B}'' = -2n_l^2\bar{\mathbf{A}}(\bar{\mathbf{A}}^T\bar{\mathbf{A}} + n_l\bar{\nu}\mathbf{I})^{-3}\bar{\mathbf{A}}^T \tag{59}$$

Numerical Validation

The benefits of the proposed framework are illustrated in Figures 3 and 4. A single set of 750 vertices were randomly sampled from a triangular mesh model of the asteroid Eros that has 200,700 faces. These sampled points were used to estimate spherical harmonic shape models of varying degree in three ways where all of the vertices were weighted equally. The three approaches used were least squares without regularization as shown in Eq. (43) (i.e., $\nu = 0$), the new framework described in this section with the proposed Tikhonov matrix in Eq. (47), and the new framework with a Tikhonov matrix commonly used in regularization, $\mathbf{\Gamma}^{1/2} = \mathbf{I}$. Ermakov et al. [67] found that $\alpha = 1.84$ best represents minor bodies when excluding Eros from the considered data sets. To simulate a first mission to Eros, $\alpha = 1.84$ is used throughout this paper for the Tikhonov matrix in Eq. (47) although $\alpha = 1.88$ is generally recommended for minor bodies. However, $\alpha = 1.88$ does not result in a significant difference of the estimated coefficients here. The RMS error (RMSE) between the Euclidean norms of the vertices of the triangular mesh model and the corresponding values predicted by the estimated spherical harmonic models is shown in Figure 3 for each approach. Figure 4 shows the triangular mesh shape model as well as the degree and order 16 spherical harmonic shape models estimated by each of the three approaches. Although all three approaches provide similar results for low degree spherical harmonic models, the proposed approach provides substantially better accuracy for higher degree models by preventing over fitting. Remarkably, the RMSE for the new approach with a degree and order 25 spherical harmonic model is about 2.16 times smaller than the lowest possible RMSE when using either no regularization or $\mathbf{\Gamma}^{1/2} = \mathbf{I}$.

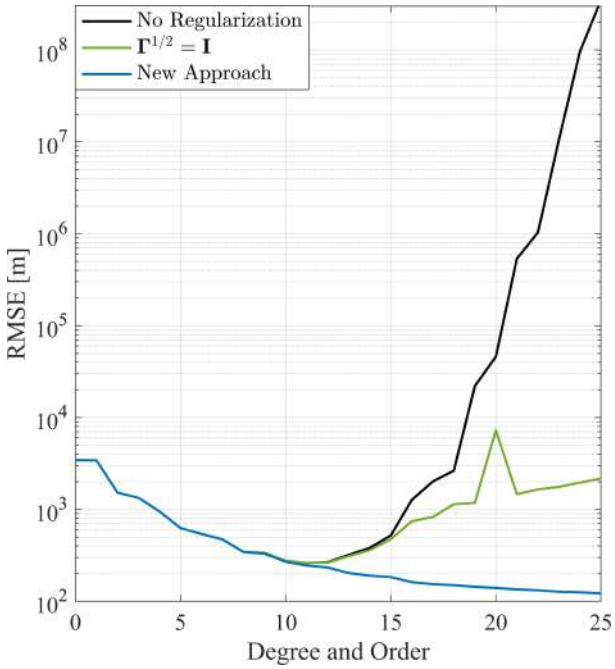

Figure 3. RMSE of estimated spherical harmonic shape models of varying degree and order as compared to a triangular mesh model.

Although the literature reports that GCV tends to work well in practice, there are cases where GCV fails, which are described in depth by Thompson et al [81]. Of most concern is when the global minimizer of $V(\bar{\nu})$ does not provide a satisfactory result. In these rare cases, GCV tends to dramatically undersmooth, which makes it easy to detect failures [76]. For the particular application of estimating spherical harmonic shape coefficients, we have found empirically that GCV is likely to fail when the landmarks are concentrated in small regions, there are large regions with relatively few or no landmarks, and a high degree spherical harmonic model is used. Thus, in practice it is recommended to employ at least one other method for choosing ν as validation. The obtained value of ν can also be validated by comparing the spectrum of the resulting estimated spherical harmonic coefficients to the a priori spectrum in Eq. (45). If the obtained ν is unsatisfactory, the degree of the spherical harmonic model should be reduced until a satisfactory ν is obtained.

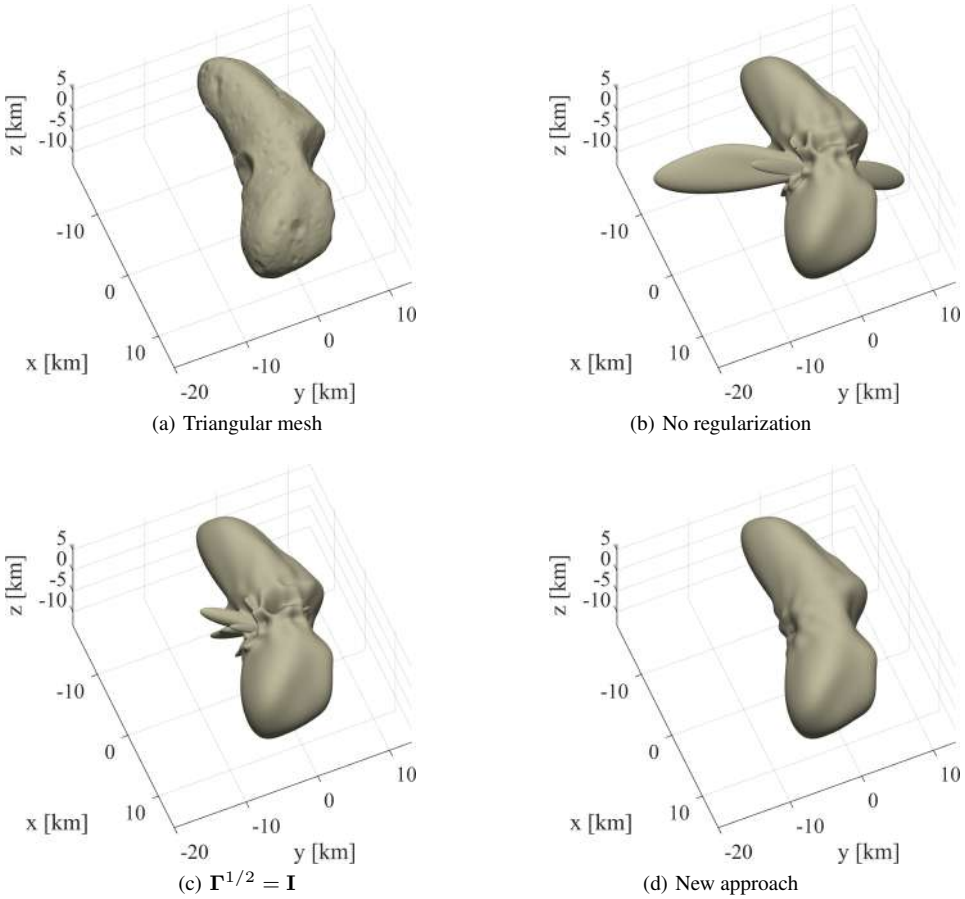

(a) Triangular mesh (b) No regularization

(c) $\mathbf{\Gamma}^{1/2} = \mathbf{I}$ (d) New approach

Figure 4. Triangular mesh model compared with estimated degree and order 16 spherical harmonic shape models using 750 vertices randomly sampled from the mesh model.

6. CASE STUDY

Orbit Geometry

The ANS architecture is validated through a MATLAB simulation of a three-spacecraft swarm orbiting the asteroid 433 Eros. Eros is used as the target asteroid because accurate shape, gravity, and rotational information is available from the NEAR Shoemaker mission [5, 12, 13]. The initial swarm mean absolute and relative orbital elements (ROE) are provided in Table 2 where the ROE are multiplied by the orbit mean semi-major axis for easy geometrical interpretation [82]. The initial mean semi-major axis of each spacecraft is 45 km, which results in an orbit period of about 25 hrs. The mean orbital elements are transformed to osculating orbital elements through the mapping described by Alfriend [83], which considers the effects of J_2. The mothership orbit is near-circular and slightly retrograde for stability [55]. The near-polar inclination also provides global coverage of the asteroid surface. The quasi-nonsingular ROE in Table 2 are defined in terms of the classic Keplerian orbital elements as

$$\begin{bmatrix} \delta a \\ \delta\lambda \\ \delta e_x \\ \delta e_y \\ \delta i_x \\ \delta i_y \end{bmatrix} = \begin{bmatrix} (a_d - a_c)/a_c \\ u_d - u_c + (\Omega_d - \Omega_c)\cos(i_c) \\ e_d\cos(w_d) - e_c\cos(w_c) \\ e_d\sin(w_d) - e_c\sin(w_c) \\ i_d - i_c \\ (\Omega_d - \Omega_c)\sin(i_c) \end{bmatrix} \tag{60}$$

Here $u = M + w$ is the mean argument of latitude, and the subscripts c and d indicate the chief and deputy respectively. The spacecraft are primarily separated in the along-track direction as described by $\delta\lambda$. The value of $\delta\lambda$ was chosen to balance the need for small intersatellite separation for satellite-to-satellite feature correlation and large intersatellite separation for passive collision avoidance, stereovision, and observability of the estimated filter state. To prevent the swarm from quickly drifting apart in the along-track direction, the initial mean relative semi-major axis δa of each deputy spacecraft relative to the mothership is zero. The details of the reference truth orbit propagations are specified in Table 3.

Table 2. Initial swarm mean absolute and relative orbital elements in the ACIC frame. The deputy ROE are defined with respect to the mothership.

	a	e	i	Ω	w	M
Mothership	45 km	0.001	110°	110°	0°	180°
	$a\delta a$	$a\delta\lambda$	$a\delta e_x$	$a\delta e_y$	$a\delta i_x$	$a\delta i_y$
Deputy 1	0 km	10 km	0 km	0 km	0 km	0 km
Deputy 2	0 km	20 km	0 km	0 km	0 km	0 km

The resulting relative motion is shown in Figure 5, which demonstrates that safe intersatellite separation is maintained. Occasional station keeping maneuvers would be required to preserve the desired relative orbit geometry. Due to perturbations from gravity coefficients other than J_2, the employed mean to osculating transformation can result in a

Table 3. Truth orbit propagation parameters.

Parameter	Value
Integration Scheme	MATLAB ode45
Initial Epoch	2000 August 1 0 hrs
Eros Gravity	Degree and order 15 [12]
Third Body Gravity	Sun point mass
Solar Radiation Pressure	S/C cross-section normal to sun, no eclipses

difference between the orbit periods of the mothership and deputies, which creates a secular drift in the spacecraft along-track separation. This phenomenon is exacerbated when decreasing the mean orbit semi-major axis, which would require a mean to osculating transformation that considers more gravity coefficients than J_2 in order to accurately match the orbit periods of the spacecraft.

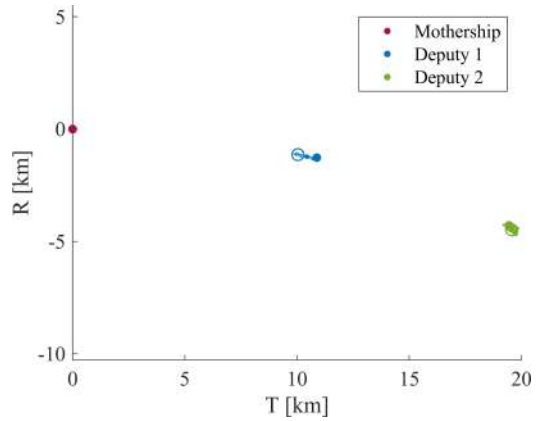

(a) Radial-transverse plane

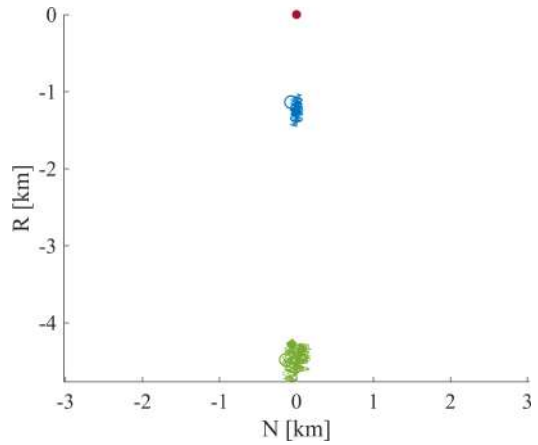

(b) Radial-normal plane

Figure 5. Motion of deputies relative to the mothership in the mothership RTN frame. The open and filled circles denote the beginning and end of the trajectories respectively.

Data Generation

Images and sensor measurements are nominally simulated every 5 min, which results in about 300 measurement intervals over an orbit period. The offset and drift of each spacecraft clock with respect to the true time is stochastically modeled according to Eq. (21) with noise parameters that are consistent with the Jackson Labs Low Power Miniature RSR CSAC [84]. For this clock, the values of q_1 and q_2 in Eq. (19) are estimated to be 6.2×10^{-21} s and 1.2×10^{-27} s^{-1} respectively using the procedure described in [58]. The measurements of each spacecraft are recorded when the nominal measurement acquisition time is reached according to the best onboard timing knowledge where the mothership clock is assumed correct. Thus, the true measurement acquisition time of each spacecraft is the desired acquisition time plus the true offset of the onboard clock relative to the true time minus the estimated offset of the onboard clock relative to the mothership clock. Images are generated in MATLAB using OpenGL, the ephemeris of Eros [85], the Eros 3D model from the NEAR Shoemaker mission [12], and the camera model in Eq. (1). The camera intrinsic parameters in Eq. (1) are consistent with the GOMSpace NanoCam with an 8 mm lens [86]. Simulated images incorporate incidence angle shading and soft shadows but no noise or skew [87,88]. In the reference truth, the attitude of each spacecraft is defined such that the CF frame z-axis points in the negative radial direction toward the asteroid center of mass, the y-axis is aligned with the orbit angular momentum vector, and the x-axis completes the right handed triad. An example of keypoint correlation between images taken by two different spacecraft at the same nominal epoch is shown in Figure 6, which also illustrates the quality of the simulated images.

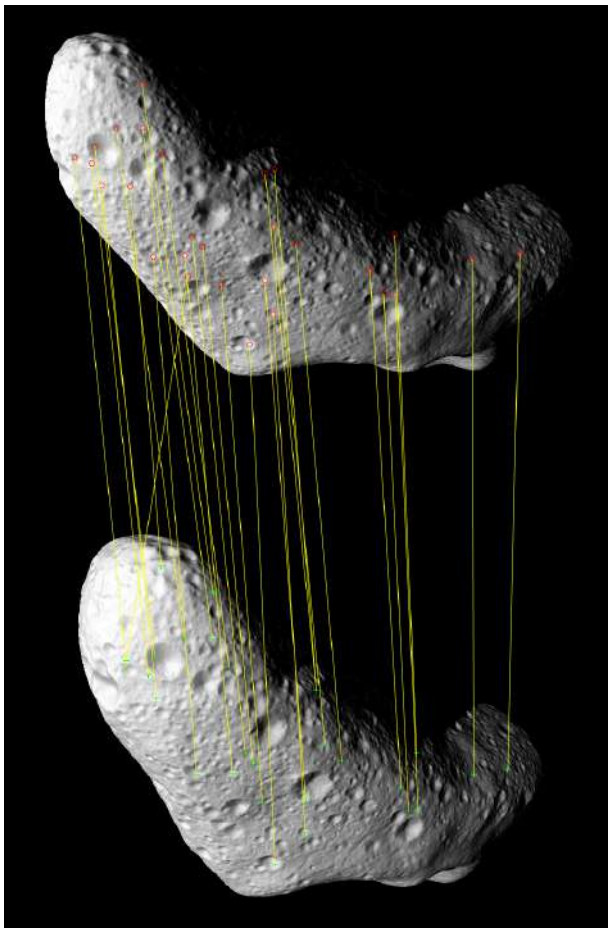

Figure 6. Intersatellite correlation between the mothership and deputy 2 using SIFT keypoint descriptors.

The intersatellite one-way pseudorange and Doppler measurements are computed according to Eqs. (33-34) and are

corrupted with zero-mean white Gaussian noise with standard deviations of 10 cm and 1 mm/s respectively. Error in the star tracker attitude solutions are simulated by multiplying each truth ACI to CF rotation matrix by a stochastic 3-1-2 Euler angle rotation sequence. The angle of each rotation is a Gaussian random variable with a standard deviation of 24 arcsec for the z-axis rotation and 7 arcsec for the x-axis and y-axis rotations, which is consistent with the noise properties of the Blue Canyon Technologies Nano-Star Camera [89].

Table 4. Landmark tracking and stereovision parameters.

Parameter	Value
Mahalanobis Threshold Probability (p_m)	0.01
Feature Descriptor Difference ($\delta_{d,t}$)	70
Mahalanobis Weight ($\hat{w}$)	20
Maximum SV Error ($P_{L,max}$)	$(1 \text{ km})^2$
Steps Before Retirement (n_r)	3
Retirement Search Distance (d_r)	0.5 km

All user-specified parameters for landmark tracking and stereovision defined in Section 3 are summarised in Table 4. Image keypoints are detected using the SIFT implementation for MATLAB from VLFeat [90]. The 100 strongest features are chosen from each image. The probability, p_m, used to define the maximum Mahalanobis distance threshold is set to 0.01, a common choice in hypothesis testing, which results in a threshold of $m_t = 3.03$. The maximum feature descriptor Euclidean distance, $\delta_{d,t}$, used for filter landmark correlation is 70. This value was chosen because landmarks with the most consecutive correlations tended to have descriptor differences in the $[5, 70]$ range in preliminary simulations. A landmark is retired from the filter state if it has not been correlated to an image keypoint for $n_r = 3$ consecutive time steps, which is 15 min. According to the previous study by the authors [37], this length of time may be enough for Lowe's keypoint matching to begin to diminish in quality. Finally, the distance to search for possible duplicates in the retired landmark database is set to 0.5 km, which is on the order of magnitude of the maximum error in stereovision estimates in preliminary simulations.

For this preliminary integration test of the proposed SNAC algorithmic framework, the stereovision algorithm utilizes the true spacecraft positions and asteroid rotational parameters corrupted with zero-mean Gaussian noise sampled according to the output filter error covariance. Thus, the stereovision estimate errors and covariances are representative, but new stereovision estimates are not correlated with the other filter state parameter estimates. The rest of the algorithms in Section 3 directly use the filter output as described in that section.

The filter a priori state uncertainty is listed in Table 6. These uncertainties are comparable to the a priori uncertainties typically used in the NEAR orbit determination [5]. The spacecraft position and velocity a priori uncertainties specified in Table 6 are in each axis. The a priori uncertainty of each normalized spherical harmonic gravity coefficient is 0.005. The error in the initial mean state estimate provided to the filter is randomly sampled according to the initial filter error covariance. The filter modeled dynamics match that of the reference truth except that the filter only estimates the spherical harmonic gravity field up to degree and order eight. Higher order degree gravity coefficients are not explicitly modeled in the filter and are captured through the filter process noise covariance. Adaptive state noise compensation is used to estimate the filter process noise covariance of the spacecraft states online through a sliding window of 50 time steps of filter output [49]. The output of filter calls where no pixel measurements are utilized is excluded from the sliding window due to the poor system observability. Equations (36-37) are used as an initial guess and upper bound of the unmodeled acceleration power spectral density. The filter measurement models are consistent with the reference truth. Lear's measurement underweighting scheme [60] is used with a factor of two for the first orbit to increase robustness to measurement nonlinearities. The modeled error standard deviation of each pixel measurement is 2 px.

Results

The error in landmark tracking and stereovision is measured by ray-tracing image points through the 3D Eros model used to generate the images. For every keypoint detected in an image, its associated ray-traced ACAF position is calculated using the true spacecraft position and attitude as well as the true asteroid state. Stereovision error is quantified as the difference between the stereovision-reconstructed ACAF position and the average of the ray-traced ACAF positions of the two keypoints used at that epoch.

Filter to spacecraft landmark correlation (step one in Section 3) error is computed as the difference between the estimated ACAF position used for correlation at that time step and the average ray-traced ACAF position of the landmark the first time it was observed. The ray-traced position from the first observation is used because correlation may select a point next to, but still within the covariance bounds of the filter landmark, which could lead to drift in the filter landmark over time. Spacecraft to spacecraft correlation (step two of Section 3) error is quantified as the difference between the ray-traced ACAF positions of the two keypoints at that time step.

Table 5 shows the mean and standard deviation of the tracking and stereovision errors along with the mean and standard deviation for the accepted Mahalanobis distances m_{ik^*} and feature descriptor differences $\|\boldsymbol{d}_i - \boldsymbol{d}_{k^*}\|_2$ and $\|\boldsymbol{d}_{k1} - \boldsymbol{d}_{k2}\|_2$. The tracking and stereovision errors are denoted $[\delta_x, \delta_y, \delta_z]^T$ and are expressed in the CF frame of the observing spacecraft. The errors are small relative to the average radius of Eros, 8420 m, with the exception of the z-axis for stereovision and filter to spacecraft landmark correlation. For reference, the standard deviations of the stereovision z and y errors as a percent of the average radius of Eros are 2.7% and 0.33% respectively. Stereovision estimates the depth of each pair of points along the z-axis so it is expected that stereovision and, consequently, the filter landmarks have the most error in the z-direction. Figure 7 shows the average stereovision error per time step over the first three orbits. The stereovision errors tend to decrease over time as the uncertainty in the filter state decreases.

Interestingly, the error standard deviations in the x-direction are slightly larger than the errors in the y-direction for both tracking methods and stereovision because they are compounded by spacecraft to spacecraft correlation. Spacecraft to spacecraft correlation does not use any state estimates to perform matching, which isolates it from the systematic depth errors experienced by stereovision and filter to spacecraft correlation. Because the spacecraft are separated in the CF frame x-direction but not in the y-direction, spacecraft to spacecraft correlation mostly induces errors along the x-axis. This error is propagated directly to the stereovision

Table 5. Statistics for filter to spacecraft (F2SC) correlation metrics, spacecraft to spacecraft (SC2SC) correlation metrics, and stereovision (SV) estimates. Position errors are in the CF frame of the observing spacecraft.

	Parameter	μ	σ
F2SC	δ_x [m]	-0.8133	43.81
	δ_y [m]	0.4047	35.50
	δ_z [m]	-23.63	185.6
	m_{ik^*}	0.4310	0.4192
	$\|\boldsymbol{d}_i - \boldsymbol{d}_{k^*}\|_2$	52.89	11.46
SC2SC	δ_x [m]	-7.589	57.36
	δ_y [m]	-0.1398	34.21
	δ_z [m]	0.1297	71.63
	$\|\boldsymbol{d}_{k1} - \boldsymbol{d}_{k2}\|_2$	88.09	48.04
SV	δ_x [m]	-4.183	50.81
	δ_y [m]	-0.6674	27.44
	δ_z [m]	-21.18	230.6

estimates. The mean descriptor difference is higher for spacecraft to spacecraft correlation than for filter to spacecraft correlation. This could be for two reasons. One, spacecraft to spacecraft correlation compares two different cameras and camera perspectives while filter to spacecraft correlation typically compares descriptors between landmarks observed by the same camera. Two, filter to landmark correlation incorporates Mahalanobis distance as an additional metric for pair rejection.

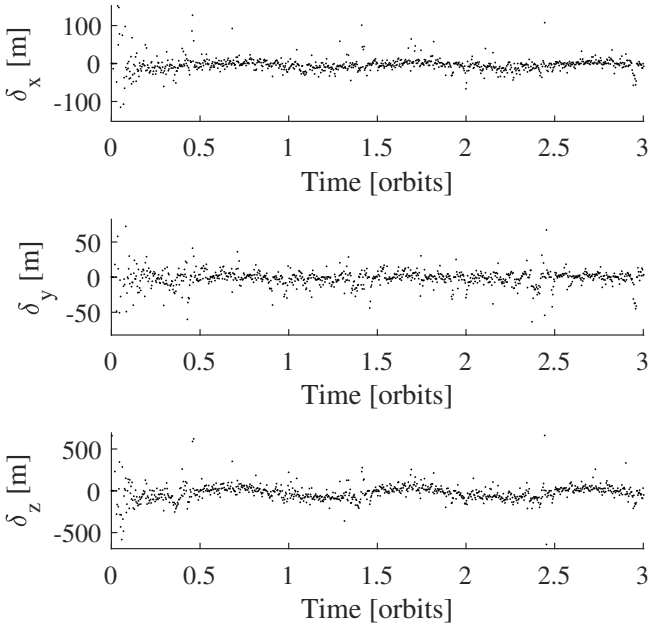

Figure 7. Error in stereovision estimates over the first three orbits, expressed in the camera frame of the observing spacecraft. Each subplot's y-axis is cropped to the respective 3σ bound from Table 5 to make trends more visible.

The distribution of the number of time steps for which each landmark was correlated to a keypoint in at least one spacecraft image is shown in Figure 8. Of these landmarks, about 49% were correlated for at least three time steps. The final database of landmarks is displayed in Figure 11(b). There is a relatively even distribution of landmarks across the surface of Eros with few outliers. The distribution of the final database shows that the landmark tracking and stereovision subsystem and state estimation subsystem worked well together to refine the majority of the stereovision estimates to the surface of Eros.

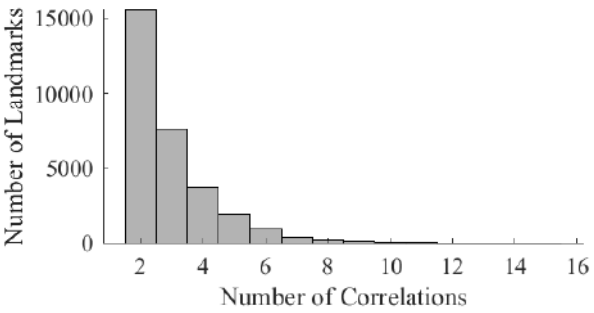

Figure 8. Histogram of the number of time steps for which each landmark was correlated to a keypoint in at least one spacecraft image.

Filter performance is shown in Figure 9 and Table 6. Figure 9 shows qualitative filter convergence behavior for several state parameters. The filter initially converges very rapidly but remains consistent. Table 6 shows quantitative filter performance using two error metrics. The first metric is the RMSE where the error is the difference between the true and estimated state parameters. In computing the RMSE of the specified parameter, all the errors of each state element associated with that parameter are considered over the final orbit of simulation. For example, the provided spacecraft position RMSE considers the position errors in each axis for each spacecraft. The second performance metric in Table 6, denoted $\bar{\sigma}$, is the square root of the mean variance provided by the filter. Similar to the RMSE, $\bar{\sigma}$ considers the variances of each state element associated with that parameter over the final orbit of simulation.

The RMSE and $\bar{\sigma}$ in Table 6 are similar for each parameter. The fact that the filter provided formal uncertainties are consistent with the true errors indicates the filter is functioning well. Furthermore, the a priori uncertainty of each parameter is significantly reduced by the end of the simulation. In particular, the uncertainty of the asteroid gravitational parameter is reduced by three orders of magnitude. The accuracy in estimating the spherical harmonic gravity field is illustrated in Figure 10. This figure shows that the asteroid gravity spherical harmonic coefficients were estimated to an uncertainty approximately equal to or less than the magnitude of the true coefficients up through degree and order six. Again, the estimation errors are consistent with the filter formal uncertainties.

A degree and order ten shape model was fit to the final landmark database. Then a simple approach was employed to remove salient outliers. Any landmark estimate whose radius was greater than 1.2 times the radius predicted by the spherical harmonic shape model was removed from the database. This resulted in the removal of seven large outliers not shown in Figure 11(b). Then a degree and order ten shape model was fit to the updated landmark database, and is shown in Figure 11. The RMSE between the Euclidean norms of the vertices of the truth shape model and the corresponding values predicted by the estimated spherical harmonic model is 294 m, which is 3.5% of the true asteroid average radius

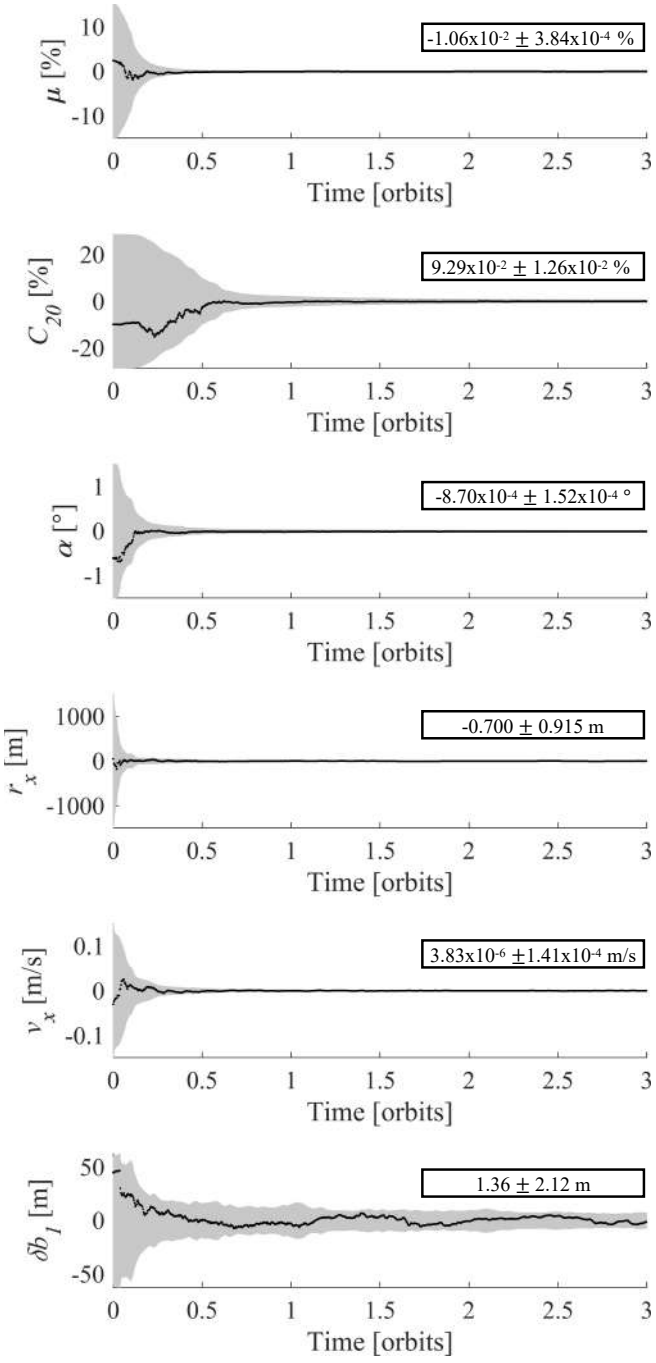

Figure 9. Filter estimation error and associated 3-σ formal uncertainty bound over first three orbits. From top to bottom, considered state parameters are asteroid gravitational parameter, $C_{2,0}$ spherical harmonic gravity coefficient, and spin axis right ascension followed by x-components of the chief position and velocity vectors and offset of first deputy clock relative to the mothership clock multiplied by the speed of light. Boxed numbers are error mean and standard deviation over last orbit of simulation.

[91]. More accurate shape reconstruction can likely be achieved through additional orbits of observations and more sophisticated outlier rejection methods.

The filter computation time is heavily dominated by the orbit propagations in the time update. Reducing the number of orbit propagations through the ETS technique significantly decreases the filter computation time. When using ETS, the number of orbit propagations in the time update does not depend on the number of landmarks in the estimated state. Thus, ETS provides a greater percent reduction in filter computation time over a traditional UKF when more landmarks are included in the estimated state. When there are no landmarks or 150 landmarks in the estimated state, ETS reduces the filter computation time by about 11% and 83% respectively as compared to a traditional UKF.

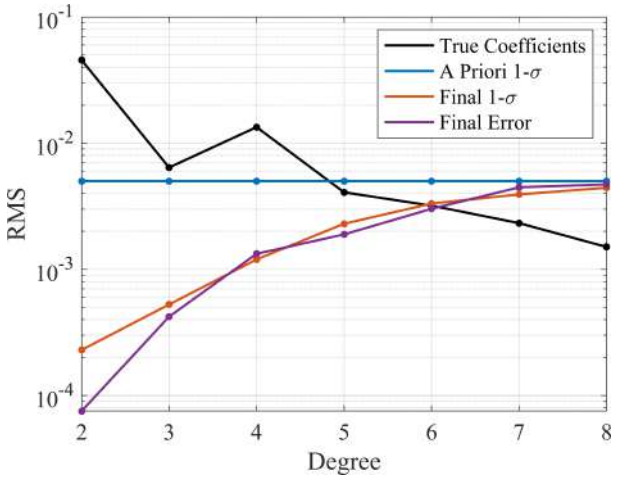

Figure 10. Comparison of the RMS of each degree of the true spherical harmonic gravity coefficients, the $1-\sigma$ a priori uncertainty provided to the filter, and the estimation error and $1-\sigma$ uncertainty at the end of the simulated case study.

7. Conclusions

Completed asteroid missions have required extensive human oversight and use of ground-based resources such as the NASA Deep Space Network. In contrast, this paper develops an autonomous asteroid characterization algorithmic framework for the Autonomous Nanosatellite Swarming (ANS) mission concept. Specifically, the novel ANS simultaneous navigation and characterization (SNAC) architecture is addressed. SNAC is a new class of estimation problem defined in this paper as a superset of simultaneous localization and mapping. For ANS, SNAC includes estimating the spacecraft states as well as the asteroid gravity field, rotational motion, and shape. Through autonomy and small satellite technology, ANS improves performance and reduces mission cost, which enables a greater number of future asteroid missions.

ANS comprises a mothership and one or more smaller nanosatellites in closed orbits equipped with low size, weight, power, and cost avionics. Stereovision and optical feature tracking algorithms are utilized in a novel manner to provide initial estimates of asteroid landmark positions and optical pixel measurements of these landmarks over time. The optical landmark measurements are fused with intersatellite radio-frequency measurements in a computationally efficient and robust unscented Kalman filter to simultaneously estimate the spacecraft states and the asteroid gravity field, rotational motion, and landmark positions. The estimated landmark positions are utilized to reconstruct a global spherical harmonic asteroid shape model through a new technique that leverages a priori knowledge of the shape characteristics of small celestial bodies.

Table 6. Comparison of the a priori filter state uncertainty with the estimation performance over the final orbit of simulation. Percentages refer to percent of the true value.

	Parameter	A Priori 1-σ	Filter RMSE	Filter $\bar{\sigma}$
Asteroid	μ [%]	5	1.06×10^{-2}	6.98×10^{-3}
	α [°]	0.5	1.54×10^{-5}	4.72×10^{-5}
	δ [°]	0.5	8.43×10^{-6}	4.02×10^{-5}
	w [%]	1×10^{-3}	3.76×10^{-6}	6.80×10^{-7}
Spacecraft	Position [m]	500	2.69	1.22
	Velocity [mm/s]	50	0.167	0.101
	C_R [%]	10	1.41	1.35
	b_R [m]	20	3.19	1.98
	b_D [mm/s]	2	0.475	0.421

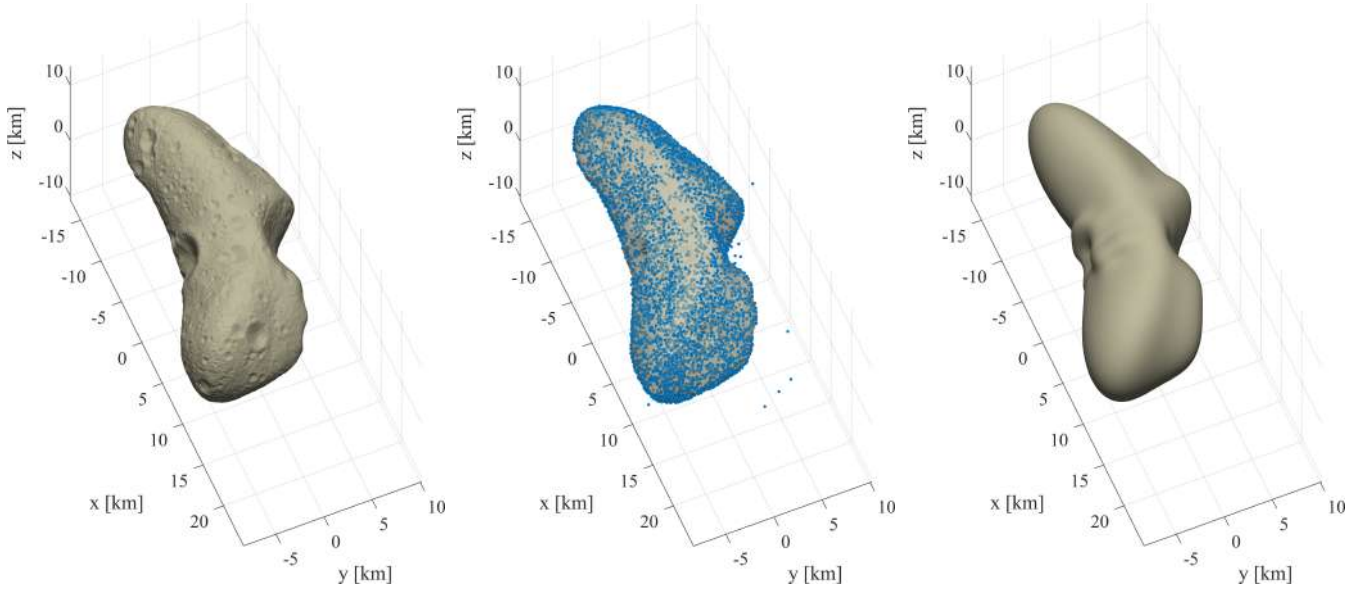

(a) True Shape Model (b) Landmark Database (c) Global Shape Reconstruction

Figure 11. Comparison of a) the true asteroid shape model used to generate images in the simulation, b) the final landmark database plotted with the true shape model made transparent, and c) the estimated degree and order ten spherical harmonic shape model.

High-fidelity numerical simulations of three spacecraft orbiting the asteroid 433 Eros demonstrate that ANS achieves safe and accurate SNAC. The designed orbit geometry provides passive safety throughout the simulation and results in inter-satellite separations that are small enough for SIFT feature correlation between spacecraft and large enough for accurate stereovision. The stereovision errors in the depth direction are generally less than 9% of the average asteroid radius. Landmark tracking errors are less than 2% of the average asteroid radius in the non-depth directions. After just ten orbits, the uncertainty in every filter state parameter is reduced significantly. Specifically, the asteroid gravity spherical harmonic coefficients were estimated to an uncertainty approximately equal to or less than the magnitude of the true coefficients up through degree and order six. Furthermore, the novel spherical harmonic global shape estimation technique was able to reconstruct the shape of Eros with an RMSE of 3.5% of the average asteroid radius.

The most important future work is to validate the complete integration of the proposed SNAC algorithmic framework by directly using the filter output for stereovision. Stereovision can likely be improved by incorporating random sample consensus or another outlier rejection method in spacecraft to spacecraft keypoint correlation. Other important future work includes testing the developed framework with hardware in the loop. Specifically, the ANS SNAC architecture will be validated using images produced by the Stanford Space Rendezvous optical stimulator and robotic testbed for rendezvous and optical navigation. The algorithms should also be profiled on representative flight hardware to ensure the computational load can be reasonably accommodated onboard. Further work should investigate sequentially estimating or updating the global shape model. Furthermore, it should be determined if the global shape model can be leveraged to improve landmark detection and tracking and to aid in trajectory planning by identifying areas of high shape uncertainty that require further observations.

ACKNOWLEDGMENTS

This work is supported by the NASA Small Spacecraft Technology Program cooperative agreement number 80NSSC18M0058 for contributions to the Autonomous Nanosatellite Swarming (ANS) Using Radio-Frequency and Optical Navigation project. The authors thank the Achievement Rewards for College Scientists (ARCS) Foundation for the provided fellowship financial support. The authors also thank Corinne Lippe of the Stanford Space Rendezvous Laboratory (SLAB) for her contributions to the reference truth orbit propagator.

REFERENCES

[1] Committee on the Planetary Science Decadel Survey, Space Studies Board, Division on Engineering and Physical Sciences, and National Research Council of the National Academies, *Vision into Voyages for Planetary Science in the Decade 2013-2022*. The National Academies Press, 2011.

[2] E. Anders, "Pre-biotic organic matter from comets and asteroids," *Nature*, vol. 342, no. 6247, pp. 255–257, Nov. 1989.

[3] A. Coradini, D. Turrini, C. Federico, and G. Magni, "Vesta and Ceres: Crossing the history of the solar system," *Space Science Reviews*, vol. 163, no. 1, pp. 25–40, 2011.

[4] E. Adams, D. O'Shaughnessy, M. Reinhart, J. John, E. Congdon, D. Gallagher, E. Abel, J. Atchison, Z. Fletcher, M. Chen, C. Heistand, P. Huang, E. Smith, D. Sibol, D. Bekker, and D. Carrelli, "Double asteroid redirection test: The earth strikes back," in *2019 IEEE Aerospace Conference*, 2019.

[5] B. G. Williams, "Technical challenges and results for navigation of NEAR shoemaker," *Johns Hopkins APL Technical Digest*, vol. 23, no. 1, 2002.

[6] A. S. Konopliv, S. W. Asmar, B. G. Bills, N. Mastrodemos, R. S. Park, C. A. Raymond, D. E. Smith, and M. T. Zuber, "The Dawn gravity investigation at Vesta and Ceres," *Space Science Reviews*, vol. 163, no. 1, pp. 461–486, 2011.

[7] D. S. Lauretta, S. S. Balram-Knutson, E. Beshore, W. V. Boynton, C. Drouet d'Aubigny, D. N. DellaGiustina, H. L. Enos, D. R. Golish, C. W. Hergenrother, E. S. Howell, C. A. Bennett, E. T. Morton, M. C. Nolan, B. Rizk, H. L. Roper, A. E. Bartels, B. J. Bos, J. P. Dworkin, D. E. Highsmith, D. A. Lorenz, L. F. Lim, R. Mink, M. C. Moreau, J. A. Nuth, D. C. Reuter, A. A. Simon, E. B. Bierhaus, B. H. Bryan, R. Ballouz, O. S. Barnouin, R. P. Binzel, W. F. Bottke, V. E. Hamilton, K. J. Walsh, S. R. Chesley, P. R. Christensen, B. E. Clark, H. C. Connolly, M. K. Crombie, M. G. Daly, J. P. Emery, T. J. McCoy, J. W. McMahon, D. J. Scheeres, S. Messenger, K. Nakamura-Messenger, K. Righter, and S. A. Sandford, "OSIRIS-REx: Sample return from Asteroid (101955) Bennu," *Space Science Reviews*, vol. 212, no. 1, pp. 925–984, Oct. 2017.

[8] T. Hashimoto, T. Kubota, J. Kawaguchi, M. Uo, K. Shirakawa, T. Kominato, and H. Morita, "Vision-based guidance, navigation, and control of Hayabusa spacecraft - Lessons learned from real operation," *IFAC Proceedings Volumes*, vol. 43, no. 15, pp. 259–264, 2010.

[9] S. Watanabe, Y. Tsuda, M. Yoshikawa, S. Tanaka, T. Saiki, and S. Nakazawa, "Hayabusa2 Mission Overview," *Space Science Reviews*, vol. 208, no. 1, pp. 3–16, Jul. 2017.

[10] N. Stacey and S. D'Amico, "Autonomous swarming for simultaneous navigation and asteroid characterization," in *2018 AIAA/AAS Astrodynamics Specialist Conference*, Snowbird, UT, 2018.

[11] S. Thrun, W. Burgard, and D. Fox, *Probabilistic Robotics*. The MIT Press, 2005, pp. 65–71.

[12] A. Konopliv, J. Miller, W. Owen, D. Yeomans, and J. Giorgini, "A global solution for the gravity field, rotation, landmarks, and ephemeris of Eros," *Icarus*, vol. 160, no. 2, pp. 289–299, 2002.

[13] J. K. Miller, A. S. Konopliv, P. G. Antreasian, J. J. Bordi, S. Chesley, C. E. Helfrich, W. M. Owen, T. C. Wang, B. G. Williams, D. K. Yeomans, and D. J. Scheeres, "Determination of shape, gravity, and rotational state of asteroid 433 Eros," *Icarus*, vol. 155, no. 1, 2002.

[14] R. W. Gaskell, O. S. Barnouin-Jha, D. J. Scheeres, A. S. Konopliv, T. Mukai, S. Abe, J. Saito, M. Ishiguro, T. Kubota, T. Hashimoto, J. Kawaguchi, M. Yoshikawa, K. Shirakawa, T. Kominato, N. Hirata, and H. Demura, "Characterizing and navigating small bodies with imaging data," *Meteoritics & Planetary Science*, vol. 43, no. 6, pp. 1049–1061, Jun. 2008.

[15] N. Mastrodemos, B. Rush, A. Vaughan, and O. William Jr, "Optical navigation for the Dawn mission at Vesta," Oct. 2012.

[16] M. T. Zuber, D. E. Smith, M. M. Watkins, S. W. Asmar, A. S. Konopliv, F. G. Lemoine, H. J. Melosh, G. A. Neumann, R. J. Phillips, S. C. Solomon, M. A. Wieczorek, J. G. Williams, S. J. Goossens, G. Kruizinga, E. Mazarico, R. S. Park, and D.-N. Yuan, "Gravity field of the Moon from the gravity recovery and interior laboratory (GRAIL) mission," *Science*, vol. 339, no. 6120, pp. 668–671, Feb. 2013.

[17] J. Leonard, B. Jones, E. Villalba, and G. Born, "Absolute Orbit Determination and Gravity Field Recovery for 433 Eros Using Satellite-to-Satellite Tracking," in *AIAA/AAS Astrodynamics Specialist Conference*, 2012.

[18] S. Hesar, J. Parker, J. McMahon, and G. Born, "Small body gravity field estimation using LIAISON supplemented optical navigation," in *AAS GN&C Conference*, 2015.

[19] S. Bhaskaran, S. Nandi, S. Broschart, M. Wallace, L. A. Cangahuala, and C. Olson, "Small body landings using autonomous onboard optical navigation," *The Journal of the Astronautical Sciences*, vol. 58, no. 3, pp. 409–427, Jul. 2011.

[20] K. Fujimoto, N. Stacey, and J. M. Turner, "Stereoscopic image velocimetry as a measurement type for autonomous asteroid gravimetry," in *2016 AIAA/AAS Astrodynamics Specialist Conference*, 2016.

[21] J. A. Atchison, R. H. Mitch, C. Apland, C. L. Kee, and K. W. Harclerode, "Small body in-situ multi-probe mass estimation experiment (SIMMEE)," in *2017 IEEE Aerospace Conference*.

[22] J. Atchison et al., "Swarm flyby gravimetry," *The Johns Hopkins University Applied Physics Laboratory, NIAC Phase II Final Report*, 2017.

[23] A. F. J. H. Marco Pavone, Julie Castillo-Rogez and I. Nesnas, "Spacecraft/rover hybrids for the exploration of small solar system bodies," *NIAC Phase II Final Report*, 2017.

[24] B. Hockman, "Gravity poppers: Hopping probes for the interior mapping of small solar system bodies," *NIAC Phase I Final Report*, 2020.

[25] Y. Cheng and J. K. Miller, "Autonomous landmark based spacecraft navigation system," Ponce, Puerto Rico, Feb. 2003.

[26] B. D. Tapley, S. Bettadpur, M. Watkins, and C. Reigber, "The gravity recovery and climate experiment: Mission overview and early results," *Geophysical Research Letters*, vol. 31, no. 9, 2004.

[27] G. Krieger, A. Moreira, H. Fiedler, I. Hajnsek, M. Werner, M. Younis, and M. Zink, "Tandem-x: A satellite formation for high-resolution sar interferometry," *IEEE Transactions on Geoscience and Remote Sensing*, vol. 45, no. 11, pp. 3317–3341, 2007.

[28] J. L. Burch, T. E. Moore, R. B. Torbert, and B. L. Giles, "Magnetospheric multiscale overview and science objectives," *Space Science Reviews*, vol. 199, no. 1, pp. 5–21, Mar. 2016.

[29] H. Sanchez, D. McIntosh, H. Cannon, C. Pires, J. Sullivan, B. O'Connor, and S. D'Amico, "Starling1: Swarm technology demonstration," in *32nd Annual Small Satellite Conference, AIAA/USU*, 2018.

[30] S. D'Amico, A. Koenig, B. Macintosh, and D. Mauro, "System design of the miniaturized distributed occulter/telescope (mdot) science mission," in *33rd Annual Conference on Small Satellites*, 2019.

[31] S. Palo, M. Pilinski, J. Thayer, W. Lohmeyer, K. Lemmer, S. D'Amico, G. Lightsey, and S. Latif, "The space weather atmospheric reconfigurable multiscale experiment (swarm-ex): A new nsf supported cubesat project," in *American Geophysical Union, Fall Meeting*, 2020.

[32] A. Koenig, S. D'Amico, and E. Lightsey, "Formation flying orbit and control concept for the visors mission," in *AIAA Scitech 2021 Forum*, 2021.

[33] A. T. Klesh, B. Clement, C. Colley, J. C. Essmiller, D. Forgette, J. Krajewski, A. D. Marinan, and T. J. Martin-Mur, "Marco: Early operations of the first cubesats to mars," in *32nd Annual AIAA/USU Conference on Small Satellites*, 2018.

[34] V. Giralo and S. D'Amico, "Distributed multi-GNSS timing and localization for nanosatellites," *Navigation*, vol. 66, no. 4, pp. 729–746, 2019.

[35] J. Kruger, K. Wallace, A. Koenig, and S. D'Amico, "Autonomous angles-only navigation for spacecraft swarms around planetary bodies," in *2021 IEEE Aerospace Conference*, 2021.

[36] N. Mastrodemos, D. G. Kubitschek, and S. P. Synnott, "Autonomous navigation for the Deep Impact mission encounter with comet Tempel 1," *Space Science Reviews*, vol. 117, no. 1, pp. 95–121, Mar. 2005.

[37] K. Dennison and S. D'Amico, "Comparing optical tracking techniques in distributed asteroid orbiter missions using ray-tracing," Charlotte, NC, Feb. 2021, virtual Event.

[38] M. Wieczorek, "Gravity and topography of the terrestrial planets," in *Treatise on Geophysics*, 2nd ed., G. Schubert, Ed. Oxford: Elsevier, 2015, pp. 153–193.

[39] R. A. Werner and D. J. Scheeres, "Exterior gravitation of a polyhedron derived and compared with harmonic and mascon gravitation representations of asteroid 4769 castalia," *Celestial Mechanics and Dynamical Astronomy*, vol. 65, no. 3, pp. 313–344, 1996.

[40] B. Yost and S. Weston, "Small spacecraft technology state of the art report, nasa/tp-20210021263," *Small Spacecraft Systems Virtual Institute*, 2021.

[41] C. Lippe and S. D'Amico, "Spacecraft swarm dynamics and control about asteroids," *Advances in Space Research*, Jul. 2020.

[42] D. G. Lowe, "Distinctive image features from scale-invariant keypoints," *International Journal of Computer Vision*, vol. 60, no. 2, pp. 91–110, Nov. 2004.

[43] N. Takeishi, A. Tanimoto, T. Yairi, Y. Tsuda, F. Terui, N. Ogawa, and Y. Mimasu, "Evaluation of interest-region detectors and descriptors for automatic landmark tracking on asteroids," *Transactions of the Japan Society for Aeronautical and Space Sciences*, vol. 58, no. 1, pp. 45–53, 2015.

[44] R. Hartley and A. Zisserman, *Multiple view geometry in computer vision*. Cambridge: Cambridge University Press, 2004.

[45] M. J. Schuster, K. Schmid, C. Brand, and M. Beetz, "Distributed stereo vision-based 6D localization and mapping for multi-robot teams," *Journal of Field Robotics*, vol. 36, no. 2, pp. 305–332, Mar. 2019, publisher: John Wiley & Sons, Ltd.

[46] P. Schmuck, "Multi-UAV collaborative monocular SLAM," *Proceedings - IEEE International Conference on Robotics and Automation*, pp. 3863–3870, 2017, iSBN: 9781509046331.

[47] S. Segal, A. Carmi, and P. Gurfil, "Stereovision-based estimation of relative dynamics between noncooperative satellites," *IEEE Transactions on Control Systems Technology*, vol. 22, no. 2, pp. 568–584, Mar. 2014.

[48] S. Watanabe, M. Hirabayashi, N. Hirata, N. Hirata, R. Noguchi, Y. Shimaki, H. Ikeda, E. Tatsumi, M. Yoshikawa, S. Kikuchi, H. Yabuta, T. Nakamura, S. Tachibana, Y. Ishihara, T. Morota, K. Kitazato, N. Sakatani, K. Matsumoto, K. Wada, H. Senshu, C. Honda, T. Michikami, H. Takeuchi, T. Kouyama, R. Honda, S. Kameda, T. Fuse, H. Miyamoto, G. Komatsu, S. Sugita, T. Okada, N. Namiki, M. Arakawa, M. Ishiguro, M. Abe, R. Gaskell, E. Palmer, O. S. Barnouin, P. Michel, A. S. French, J. W. McMahon, D. J. Scheeres, P. A. Abell, Y. Yamamoto, S. Tanaka, K. Shirai, M. Matsuoka, M. Yamada, Y. Yokota, H. Suzuki, K. Yoshioka, Y. Cho, S. Tanaka, N. Nishikawa, T. Sugiyama, H. Kikuchi, R. Hemmi, T. Yamaguchi, N. Ogawa, G. Ono, Y. Mimasu, K. Yoshikawa, T. Takahashi, Y. Takei, A. Fujii, C. Hirose, T. Iwata, M. Hayakawa, S. Hosoda, O. Mori, H. Sawada, T. Shimada, S. Soldini, H. Yano, R. Tsukizaki, M. Ozaki, Y. Iijima, K. Ogawa, M. Fujimoto, T.-M. Ho, A. Moussi, R. Jaumann, J.-P. Bibring, C. Krause, F. Terui, T. Saiki, S. Nakazawa, and Y. Tsuda, "Hayabusa2 arrives at the carbonaceous asteroid 162173 Ryugu—A spinning top–shaped rubble pile," *Science*, vol. 364, no. 6437, pp. 268–272, Apr. 2019, publisher: American Association for the Advancement of Science Section: Report.

[49] N. Stacey and S. D'Amico, "Adaptive and dynamically constrained process noise estimation for orbit determination," *IEEE Transactions on Aerospace and Electronic Systems*, 2021.

[50] S. Katz, A. Tal, and R. Basri, "Direct visibility of

point sets," in *ACM SIGGRAPH 2007 papers*, ser. SIGGRAPH '07. New York, NY, USA: Association for Computing Machinery, Jul. 2007, pp. 24–es.

[51] C. Beder and R. Steffen, "Determining an Initial Image Pair for Fixing the Scale of a 3D Reconstruction from an Image Sequence," Sep. 2006, pp. 657–666.

[52] M. Hess-Flores, S. Recker, and K. I. Joy, "Uncertainty, Baseline, and Noise Analysis for L1 Error-Based Multiview Triangulation," in *2014 22nd International Conference on Pattern Recognition*, Aug. 2014, pp. 4074–4079, iSSN: 1051-4651.

[53] S. J. Julier and J. K. Uhlmann, "New extension of the Kalman filter to nonlinear systems," *Signal Processing, Sensor Fusion, and Target Recognition VI*, vol. 3068, pp. 182–194.

[54] B. Archinal, "Report of the IAU working group on cartographic coordinates and rotational elements: 2009," *Celestial Mechanics and Dynamical Astronomy*, vol. 109, no. 2, pp. 101–135, 2011.

[55] D. J. Scheeres, *Orbital Motion in Strongly Perturbed Environments: Applications to Asteroid, Comet and Planetary Satellite Orbiters*. Springer, 2016.

[56] J. A. Burns and V. S. Safronov, "Asteroid nutation angles," *Monthly Notices of the Royal Astronomical Society*, vol. 165, p. 403, 1973.

[57] O. Montenbruck and E. Gill, *Satellite Orbits: Models, Methods and Applications*, ser. X-Pferdchen. Springer-Verlag, 2000.

[58] L. Galleani, "A Tutorial on the Two-State Model of the Atomic Clock Noise," *Metrologia*, vol. 45, no. 6, pp. S175–S182, Dec. 2008, publisher: IOP Publishing.

[59] C. Zucca and P. Tavella, "The Clock Model and its Relationship with the Allan and Related Variances," *IEEE Transactions on Ultrasonics, Ferroelectrics, and Frequency Control*, vol. 52, no. 2, pp. 289–296, Feb. 2005, conference Name: IEEE Transactions on Ultrasonics, Ferroelectrics, and Frequency Control.

[60] J. Carpenter, C. D'Souza, F. Markley, and R. Zanetti, "Navigation filter best practices," *NASA TR TP-2018-219822*, 2018.

[61] C. R. Nortje, W. O. C. Ward, B. P. Neuman, and L. Bai, "Spherical harmonics for surface parametrisation and remeshing," *Mathematical Problems in Engineering*, vol. 2015, 2015.

[62] T. C. Duxbury, "The figure of Phobos," *Icarus*, vol. 78, no. 1, pp. 169–180, 1989.

[63] D. Calvetti, S. Morigi, L. Reichel, and F. Sgallari, "Tikhonov regularization and the l-curve for large discrete ill-posed problems," *Journal of Computational and Applied Mathematics*, vol. 123, no. 1, pp. 423–446, 2000, numerical Analysis 2000. Vol. III: Linear Algebra.

[64] G. H. Golub, M. Heath, and G. Wahba, "Generalized cross-validation as a method for choosing a good ridge parameter," *Technometrics*, vol. 21, 1979.

[65] W. M. Kaula, "Determination of the Earth's gravitational field," *Reviews of Geophysics*, vol. 1, no. 4, pp. 507–551, 1963.

[66] W. Kaula, *Theory of Satellite Geodesy: Applications of Satellites to Geodesy*. Dover Publications, 2000.

[67] A. I. Ermakov, R. S. Park, and B. G. Bills, "Power laws of topography and gravity spectra of the solar system bodies," *Journal of Geophysical Research: Planets*, vol. 123, no. 8, pp. 2038–2064, 2018.

[68] A. B. Kucinskas, N. J. Borderies, and D. L. Turcotte, "Spectral study of venus global topography and geoid from Magellan and PVO data," in *Lunar and Planetary Science Conference*, ser. Lunar and Planetary Science Conference, Mar. 1993, p. 831.

[69] G. Balmino, "The spectra of the topography of the Earth, Venus and Mars," *Geophysical Research Letters*, vol. 20, no. 11, pp. 1063–1066, 1993.

[70] ——, "Gravitational potential harmonics from the shape of an homogeneous body," *Celestial Mechanics and Dynamical Astronomy*, vol. 60, no. 3, pp. 331–364, 1994.

[71] F. Vening Meinesz, "A remarkable feature of the Earth's topography," in *Proc. K. Ned. Akad. Wet. Ser. B Phys. Sci*, vol. 54, 1951, pp. 212–228.

[72] R. H. Rapp, "The decay of the spectrum of the gravitational potential and the topography for the earth," *Geophysical Journal International*, vol. 99, no. 3, pp. 449–455, Dec. 1989.

[73] P. C. Hansen, "Analysis of discrete ill-posed problems by means of the l-curve," *SIAM Review*, vol. 34, no. 4, pp. 561–580, 1992.

[74] P. C. Hansen and D. P. O'Leary, "The use of the l-curve in the regularization of discrete ill-posed problems," *SIAM Journal on Scientific Computing*, vol. 14, pp. 1487 – 1503, 1993.

[75] N. Galatsanos and A. Katsaggelos, "Methods for choosing the regularization parameter and estimating the noise variance in image restoration and their relation," *IEEE Transactions on Image Processing*, vol. 1, no. 3, pp. 322–336, 1992.

[76] A. Thompson, J. Brown, J. Kay, and D. Titterington, "A study of methods of choosing the smoothing parameter in image restoration by regularization," *IEEE Transactions on Pattern Analysis and Machine Intelligence*, vol. 13, no. 4, pp. 326–339, 1991.

[77] T. Hastie, R. Tibshirani, and J. Friedman, *The Elements of Statistical Learning*. Springer, 2017, pp. 241–245.

[78] R. L. Eubank, "Diagnostics for smoothing splines," *Journal of the Royal Statistical Society. Series B (Methodological)*, vol. 47, no. 2, pp. 332–341, 1985.

[79] J. T. Kent and M. Mohammadzadeh, "Global optimization of the generalized cross-validation criterion," *Statistics and Computing*, vol. 10, no. 3, pp. 231–236, Jul. 2000.

[80] G. H. Golub and U. von Matt, "Generalized cross-validation for large-scale problems," *Journal of Computational and Graphical Statistics*, vol. 6, no. 1, pp. 1–34, 1997.

[81] A. Thompson, J. Kay, and D. Titterington, "A cautionary note about crossvalidatory choice," *Journal of Statistical Computation and Simulation*, vol. 33, pp. 199–216, 1989.

[82] S. D'Amico, "Autonomous formation flying in low Earth orbit." Ph.D. dissertation, Delft University of Technology, 2010, OCLC: 839641932.

[83] K. Alfriend, S. Vadali, P. Gurfil, J. How, and L. Breger, *Spacecraft Formation Flying*. Elsevier, 2010, pp. 341–351.

[84] Jackson Labs. (2017) Low power miniature RSR CSAC time and frequency standard. [Online]. Available: http://www.jacksonlabs.com/index.php/products/rsr_csac_module

[85] R. Park and A. Chamberlin, "HORIZONS Web-Interface." [Online]. Available: https://ssd.jpl.nasa.gov/horizons.cgi

[86] GOMSpace. (2016) NanoCam C1U Datasheet. [Online]. Available: https://gomspace.com/shop/subsystems/payloads/earth-observation.aspx

[87] R. Siegwart, I. Nourbakhsh, and D. Scaramuzza, *Introduction to Autonomous Mobile Robots*, 2nd ed. Cambridge: Massachusetts Institute of Technology, 2004.

[88] P. S. Heckbert and M. Herf, "Simulating Soft Shadows with Graphics Hardware,," p. 10.

[89] S. Palo, G. Stafford, and A. Hoskins, "An agile multi-use nano star camera for constellation applications," in *AIAA/USU Conference on Small Satellites*, 2013.

[90] VLFeat, "VLFeat SIFT Keypoint Detection." [Online]. Available: https://www.vlfeat.org/overview/sift.html

[91] J. Giorgini. Jpl small-body database browser. Accessed: 07.09.2018. [Online]. Available: https://ssd.jpl.nasa.gov/?horizonstelnet

BIOGRAPHY

Nathan Stacey *received the B.S. degree in mechanical engineering from Utah State University, Logan, UT in 2016. In 2018, he received the M.S. degree in aeronautics and astronautics from Stanford University, Stanford, CA where he is currently pursuing the Ph.D. degree also in aeronautics and astronautics. Nathan has completed internships with the Northrop Grumman Corporation and Space Dynamics Laboratory. Presently, he is a NASA Pathways intern at Goddard Space Flight Center, Greenbelt, MD and does research in the Stanford Space Rendezvous Laboratory. His research focuses on developing advanced estimation techniques for autonomous orbit determination with application to small celestial body missions. Nathan is the 2016 Utah State University Scholar of the Year, a National Science Foundation Graduate Research Fellow, a Stanford Enhancing Diversity in Graduate Education Doctoral Fellow, and an Achievement Rewards for College Scientists Scholar.*

Kaitlin Dennison *is a Ph.D. student in the Space Rendezvous Laboratory. She received her Bachelor of Science degree in mechanical engineering from the University of Connecticut. She has completed internships at the Lawrence Livermore National Laboratory and the Air Force Research Laboratory. Kaitlin's current research focuses on autonomous feature tracking for resource-limited, distributed exploration of small bodies as part of the Autonomous Nanosatellite Swarming (ANS) project. This development will minimize the sensors necessary for robust, autonomous navigation.*

Simone D'Amico *received the B.S. and M.S. degrees from Politecnico di Milano, Milan, Italy (2003) and the Ph.D. degree from Delft University of Technology, Delft, Netherlands (2010) in aerospace engineering. He is an Associate Professor of Aeronautics and Astronautics with Stanford University, Stanford, CA, USA and a W. M. Keck Faculty Scholar in the School of Engineering. From 2003 to 2014, he was a Research Scientist and Team Leader at the German Aerospace Center (DLR), Oberpfaffenhofen, Germany. There, he gave key contributions to the design, development, and operations of spacecraft formation-flying and rendezvous missions such as GRACE (United States/Germany), TanDEM-X (Germany), PRISMA (Sweden/Germany/France), and PROBA-3 (ESA). He joined Stanford in 2014 as an Assistant Professor of Aeronautics and Astronautics and a Terman Faculty Fellow. He is the Founding Director of the Space Rendezvous Laboratory (SLAB), Stanford, CA, USA and a Satellite Advisor of the Stanford Student Space Initiative (SSI), Stanford's largest undergraduate organization. D'Amico's research aims at enabling future miniature distributed space systems for unprecedented science and exploration. His efforts lie at the intersection of advanced astrodynamics, GN&C, and space system engineering to meet the tight requirements posed by these novel space architectures. The most recent mission concepts developed by Dr. D'Amico are a miniaturized distributed occulter/telescope (mDOT) system for direct imaging of exozodiacal dust and exoplanets and the Autonomous Nanosatellite Swarming (ANS) mission for characterization of small celestial bodies. Dr. D'Amico is the Chairman of the NASA's Starshade Science and Technology Working Group (TSWG). He is a member of the advisory board of space startup companies and VC edge funds. He is a member of the Space-Flight Mechanics Technical Committee of the AAS, Associate Fellow of AIAA, Associate Editor of the AIAA Journal of Guidance, Control, and Dynamics and the IEEE Transactions of Aerospace and Electronic Systems. He is Fellow of the NAE's US FOE. He was a recipient of the Leonardo 500 Award by the Leonardo Da Vinci Society and ISSNAF (2019), the Stanford's Introductory Seminar Excellence Award (2019 and 2020), the FAI/NAA's Group Diploma of Honor (2018), the Exemplary System Engineering Doctoral Dissertation Award by the International Honor Society for Systems Engineering OAA (2016), the DLR's Sabbatical/Forschungssemester in honor of scientific achievements (2012), the DLR's Wissenschaft Preis in honor of scientific achievements (2006), and the NASA's Group Achievement Award for the Gravity Recovery and Climate Experiment, GRACE (2004).*